DOT/FAA/PM-87/21

Project Report
ATC-143

Ground Clutter Processing for Wind Measurements with Airport Surveillance Radars

M. E. Weber

4 November 1987

Lincoln Laboratory
MASSACHUSETTS INSTITUTE OF TECHNOLOGY
LEXINGTON, MASSACHUSETTS

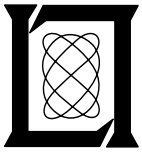

Prepared for the Federal Aviation Administration,
Washington, D.C. 20591

TECHNICAL REPORT STANDARD TITLE PAGE

1. Report No.	2. Government Accession No.	3. Recipient's Catalog No.
DOT/FAA/PM-87/21		

4. Title and Subtitle	5. Report Date
Ground Clutter Processing for Wind Measurements with Airport Surveillance Radars	4 November 1987
	6. Performing Organization Code
7. Author(s)	8. Performing Organization Report No.
Mark E. Weber	ATC-143
9. Performing Organization Name and Address	10. Work Unit No. (TRAIS)
Lincoln Laboratory, MIT P.O. Box 73 Lexington, MA 02173-0073	11. Contract or Grant No. 477/ASP-9 RADAR
	13. Type of Report and Period Covered
12. Sponsoring Agency Name and Address Department of Transportation Federal Aviation Administration 800 Independence Ave., SW Washington, DC 20591	Project Report
	14. Sponsoring Agency Code

15. Supplementary Notes

The work reported in this document was performed at Lincoln Laboratory, a center for research operated by Massachusetts Institute of Technology, under Air Force Contract F19628-85-C-0002.

16. Abstract

Modern airport surveillance radars (ASR) are coherent pulsed-Doppler radars used for detecting and tracking aircraft in terminal area air-space. These radars might serve an additional role by making radial wind measurements in the immediate vicinity of an airport to provide data on low altitude wind shear (LAWS). One factor that will affect their capability in this role is the requirement that intense low-beam ground clutter be filtered from the signals prior to estimation of the reflectivity and radial velocity of weather scatterers. This report describes and analyzes a specific signal processing algorithm for ASR weather parameter measurements. An adaptively selected Finite Impulse Response high-pass filter is used for ground clutter suppression, followed by pulse-pair weather reflectivity and radial velocity estimation. Measurements from a Lincoln Laboratory-developed testbed ASR in Huntsville, Alabama are used to characterize the ground clutter environment under siting conditions that are representative of operational ASRs. Temporal fluctuations in ground clutter intensity are analyzed with attention to their impact on the adaptive clutter-filter selection procedure. The performance of the signal processing algorithms is then analyzed using the testbed ASR ground clutter measurements in combination with simulated or real weather signals. We conclude that ground clutter and the requisite clutter filtering will not severely distort ASR wind shear measurements when the reflectivity factor of the microburst or gust front is approximately 20 dBz or greater. This is typically the case for microbursts occurring in moist conditions such as prevail over the Eastern United States during summer.

17. Key Words	18. Distribution Statement
ground clutter weather radial velocity measurement airport surveillance radar low altitude wind shear signal processing	Document is available to the public through the National Technical Information Service, Springfield, VA 22161.

19. Security Classif. (of this report)	20. Security Classif. (of this page)	21. No. of Pages	22. Price
Unclassified	Unclassified	64	

FORM DOT F 1700.7 (8-69)

Ground Clutter Processing for Wind Measurements with Airport Surveillance Radars

ABSTRACT

Modern airport surveillance radars (ASR) are coherent pulsed-Doppler radars used for detecting and tracking aircraft in terminal area air-space. These radars might serve an additional role by making radial wind measurements in the immediate vicinity of an airport to provide data on low altitude wind shear (LAWS). One factor that will affect their capability in this role is the requirement that intense low-beam ground clutter be filtered from the signals prior to estimation of the reflectivity and radial velocity of weather scatterers. This report describes and analyzes a specific signal processing algorithm for ASR weather parameter measurements. An adaptively selected Finite Impulse Response high-pass filter is used for ground clutter suppression, followed by pulse-pair weather reflectivity and radial velocity estimation. Measurements from a Lincoln Laboratory-developed testbed ASR in Huntsville, Alabama are used to characterize the ground clutter environment under siting conditions that are representative of operational ASRs. Temporal fluctuations in ground clutter intensity are analyzed with attention to their impact on the adaptive clutter-filter selection procedure. The performance of the signal processing algorithms is then analyzed using the testbed ASR ground clutter measurements in combination with simulated or real weather signals. We conclude that ground clutter and the requisite clutter filtering will not severely distort ASR wind shear measurements when the reflectivity factor of the microburst or gust front is approximately 20 dBz or greater. This is typically the case for microbursts occurring in moist conditions such as prevail over the Eastern United States during summer.

TABLE OF CONTENTS

LIST OF ILLUSTRATIONS

LIST OF TABLES

Ground Clutter Processing for Wind Measurements with Airport Surveillance Radars

I. INTRODUCTION

Lincoln Laboratory is conducting field measurements and analysis to assess the use of airport surveillance radars (ASR) for low-altitude wind shear (LAWS) measurements. It has been suggested that these radars could serve as an adjunct to a Terminal Doppler Weather Radar (TDWR) or as a stand-alone radar wind sensor at airports that will not receive a TDWR. The siting of an ASR, often at runway intersections or at one end of a major runway, might provide an improved measurement of headwind-tailwind shear when a TDWR is sited off-airport. It is unlikely that TDWRs will be deployed extensively at secondary terminals or in locales where LAWS is infrequent; at such airports an ASR could provide a capability for wind-shear detection, *albeit* with less reliability than would be provided by a TDWR. It might also be possible to improve the performance of the low-level wind shear alert system (LLWAS) by using the data from an airport surveillance radar to reduce the LLWAS false-alarm rate and to distinguish between various forms of wind shear.

In reference [1], we discussed the principal technical issues involved in low altitude wind measurement with an ASR and presented preliminary analysis of expected performance with respect to each issue. One result was that the sensitivity of ASRs is adequate to measure winds in microbursts or gust fronts at ranges less than 20 km when the associated radar reflectivity factor is 10-15 dBz or greater. This assumes that the radar is operated with an appropriate sensitivity time control (STC) function and that the "low" receiving beam is employed for wind shear measurements.

Another factor affecting the capability of ASRs to measure low-altitude wind shear is the possible error caused by weather phenomena which lie above surface boundary layer thunderstorm outflows such as "microbursts" [2]. The divergent wind pattern associated with microbursts extends only 200 - 1200 m above the surface with radial velocity at greater heights being typically of lower magnitude and/or opposite sign. Mean radial velocity measurements using an airport surveillance radar's fan-shaped elevation antenna pattern often result in an underestimate of wind shear magnitude. For very shallow thunderstorm outflows or outflows at ranges greater than 20 km, the low-altitude velocity signature of the wind shear event may not even be evident in ASR measurements. As with the system sensitivity issue, better performance in measuring LAWS would be obtained if an ASR used the low receiving beam at all ranges. We showed in reference [1] that this would extend the range for reliable measurements of microburst winds by a factor of approximately two relative to use of the high receiving beam.

Weather echoes in the low beam will be subject to significant interference from intense ground clutter in the near-airport area where wind shear measurement is operationally important. Using relatively simple signal-to-interference ratio considerations, we indicated in [1] that low-altitude wind shear events with

reflectivity factors greater than 20 dBz could be measured if clutter filter attenuation of 40 dB was combined with the use of "inter-clutter" visibility techniques.

This report considers the ground clutter processing problem in more detail, using time-series (I and Q) clutter measurements from a Lincoln Laboratory-developed testbed ASR in Huntsville, Alabama. Section II describes an initial signal-processing sequence we are using to suppress ground clutter and estimate weather reflectivity and radial velocity. Section III discusses the ground clutter environment at Huntsville and shows how spatial and temporal variations in the clutter affect the setting of signal processor parameters. In Section IV, we evaluate the clutter processing procedures using ground clutter and weather measurements from the Lincoln testbed ASR. Section V summarizes the results of this report.

II. SIGNAL PROCESSING SEQUENCE

A. Overview

Parameters of the ASR-9, the newest of the FAA's terminal radars, are outlined in Table II-1. The radar operates at S-band, featuring coherent, pulsed-Doppler processing, good sensitivity and wide dynamic range. Vertically displaced feedhorns produce two antenna patterns, shifted in elevation angle by 4.5^o. The aircraft detection channel utilizes the higher beam at short range to reduce ground clutter, with a switch over to low beam usage beyond about 10 nmi. As indicated in the introduction, reliable low-altitude wind measurements would require that a weather velocity processing channel employ the low receiving beam even at short range. In a typical operating configuration, low-beam antenna gain on the horizon would be at most 3 dB down from the peak, resulting in severe ground clutter near the radar.

Table II-1: ASR-9 Parameters

Transmitter	
Frequency	2.7-2.9 GHz
Polarization	Linear or Circular
Peak Power	1.1 MW
Pulse Width	1.0 μs
Block-Staggered CPI lengths	8 pulses/10 pulses
PRFs (Example)	972 s^{-1}/1250 s^{-1}
Receiver	
Noise Figure	4.1 dB (max)
Sensitivity	-108 dBm
A/D Word Size	12 bit
Antenna	
Elevation Beamwidth	4.8^o (min)
Azimuth Beamwidth	1.4^o
Power Gain	34 dB
Rotation Rate	12.5 RPM

One method for extracting weather information in the presence of ground clutter utilizes a high-pass prefilter to eliminate low Doppler ground echoes. Weather parameter estimates are then formed at the filter output under the assumption that the filter removes negligible power from the spectrum component produced by weather. This assumption is generally valid for slow scanning meteorological radars where the clutter spectrum width is narrow in comparison to weather spectrum width, and where sharp high-pass filters can be designed using long coherent processing intervals (CPI).

As seen from Table II-1, ASRs scan azimuthally at 75^o per second, transmitting only about 18 pulses during the interval in which the antenna scans one beamwidth. In order to reduce aircraft "blind speeds", this short data sequence is further broken up into two blocks consisting of eight pulses at a "low" PRF followed by ten pulses at a "high" PRF . In contrast to most weather radars, the scan-modulated spectrum width of ASR ground clutter (σ_V(clutter) = 0.75 m/s) would often be comparable to the weather spectrum width. In addition, high-pass filters designed to the short available CPIs will necessarily have broad transition bands if the required clutter suppression is to be achieved. As a result of these two factors, an airport surveillance radar's ground clutter prefilter might remove a

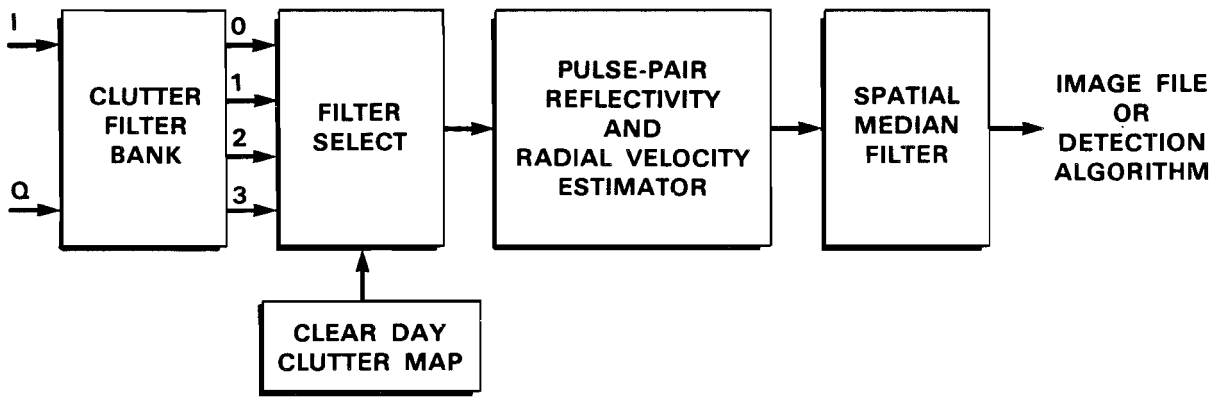

Figure II-1. Block diagram of signal processing for ASR wind measurement.

substantial amount of power from the weather echo -- resulting in significant weather parameter estimate biases -- unless the transfer function is approximately matched to the inverse of the scan-modulated clutter plus noise spectrum.

A straightforward method for approximately matching the filter transfer function to the ground clutter spectrum is illustrated in Figure II-1. A bank of prefilters run in parallel to provide transfer functions that vary from all-pass to a notch sufficiently wide to provide clutter attenuation matched to the strongest ground echoes. A "clear day map" stores *a priori* information on the spatial distribution of clutter residues associated with each filter. This map is compared to the filter outputs to select that filter which provides sufficient, but not excessive clutter attenuation. The selection process operates independently for each range/azimuth cell.

Reflectivity and mean radial velocity estimates are formed using the pulse-pair algorithm applied to the filter output samples. As will be shown in subsequent discussion, ground clutter "breakthrough" probability is significantly reduced by a nine-nearest-neighbor spatial median filter at the output of the pulse-pair processor.

The clutter processing sequence outlined in Figure II-1 was chosen for ease of implementation and proven performance capability (an analogous configuration used in the ASR-9's six-level reflectivity processor has been previously evaluated in simulation studies [3]). While this processor is in no sense optimal, we believe that the key element of the sequence -- use of *a priori* information on the ground clutter distribution -- will be a central feature of any subsequent clutter rejection algorithms for ASR weather processors. Features of the ground clutter considered in this report, such as temporal variability and the spatial correlation of intensity fluctuations, should therefore be considered as applicable well beyond the specific signal processing sequence considered here.

B. Clutter Filter Design

The clutter filters operate according to a scheme proposed by Anderson [4], involving coherent processing across the ASR-9's PRF staggers to produce a longer CPI. The finite impulse response (FIR) filters have 17 coefficients, approximately matched to the number of pulses transmitted during a beam dwell. Longer filters would realize little additional gain owing to decorrelation between data samples in the filter window. The filters are convolved with pulses from three successive CPIs (approximately 26 pulses) resulting in 10 filtered output samples not contaminated by "edge" effects. Figure II-2 illustrates the technique.

Anderson [4] showed that a small degradation in clutter suppression capability resulted when shift-invariant FIR filters operate across the PRF stagger. This degradation can be eliminated by allowing the filters to be shift-variant. A simple design technique involves the "cascade" of a shift-variant interpolation filter with a standard Tchebyshev optimal high-pass filter. The first stage interpolates the data to an equal spaced sampling grid (at the average PRI, τ) and the second stage provides the clutter suppression.

We define the interpolator's impulse response as:

$$h(p,n) \qquad p=-P,P \tag{1}$$

where n indexes the output time $n\tau$. If the high-pass filter's impulse response is:

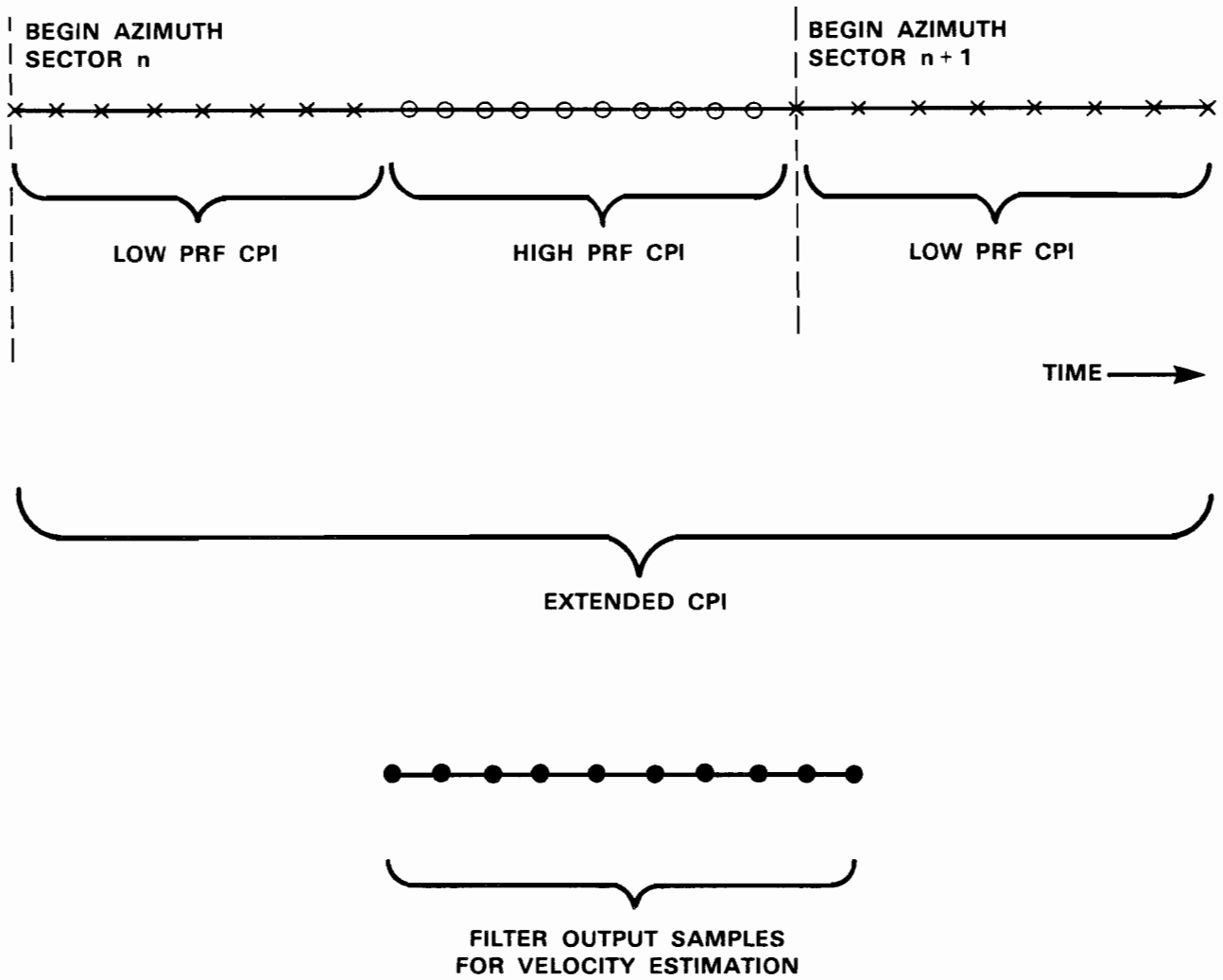

Figure II-2. Illustration of multiple-CPI clutter filtering technique.

$$u(k) \qquad k=-K,K \tag{2}$$

and x(n) is the unequal-spaced input data sequence, it is readily shown that the interpolated, high-pass filtered output sequence is given by:

$$y(n)=\sum_{m=-K-P}^{K+P} g(m,n)x(n-m) \tag{3}$$

The composite impulse response is:

$$g(m,n)=\sum_{k}\sum_{p\epsilon p\equiv m-k} u(k)h(p,n-k) \tag{4}$$

In our design the interpolation filter effects a piecewise Bessel interpolation [5], using the four nearest data samples to the output grid point. The high-pass filter is designed using the Parks-McClellan computer algorithm [6].

A shift-dependent transfer function for such a filter can be defined by the magnitude and phase of the filter outputs for unit amplitude complex sinusoidal inputs. An example of this transfer function is shown in Figures II-3(a) and (b) for a representative output point (n = 10). For comparison, the magnitude of the transfer function of the equal-spaced high-pass clutter filter is drawn with a dashed line. The magnitude response of the shift-variant clutter filter is almost indistinguishable from that of the original filter. The phase response shows only slight departures from linearity.

Figure II-3(c) is the time-averaged magnitude response over the set of output data points that would be used for pulse-pair estimation. (The filter's impulse response length is 17 so output points 8 through 17 are free of edge effects.) For comparison, Figure II-3(d) plots the corresponding transfer function when the interpolation stage is not included in the filter design. In the latter case, the PRF stagger causes some degradation in the stop-band response, resulting in a 3.6 dB reduction in achieved clutter attenuation.

C. Fill Pulses

The antenna rotation rate of an airport surveillance radar may vary by ±10% owing to wind loading. To maintain scan-to-scan azimuthal synchronization for the target channel signal processor, a variable number of "fill" pulses are added to the nominal 8/10 pulse CPI sequence. Thus in the pulse transmission sequence illustration of Figure II-2, there might be from 1 to 4 low-PRF fill pulses inserted between the end of the high-PRF CPI and the azimuth sector crossing.

The effect of these fill pulses on the extended-CPI processing described above is to increase the length of the data sequence going into the shift-variant clutter filters from 26 to as much as 30. Each extended CPI will consist of 8 low-PRF pulses, 10 high-PRF pulses, and finally from 8 to 12 low-PRF pulses. The shift variant clutter filters are simply designed with enough terms to accommodate the longest possible sequence. Since the PRF staggers will always occur at the same sample indices within the sequence, the filter coefficients for the first 10 (see Figure II-2) output data points are independent of the number of fill pulses. The presence of fill pulses simply increases the number of usable data samples at the clutter filter outputs.

The number of fill pulses transmitted during generation of the clutter residue map may differ from the number transmitted during weather data collection, due to different wind loading conditions. This will not, however, significantly change

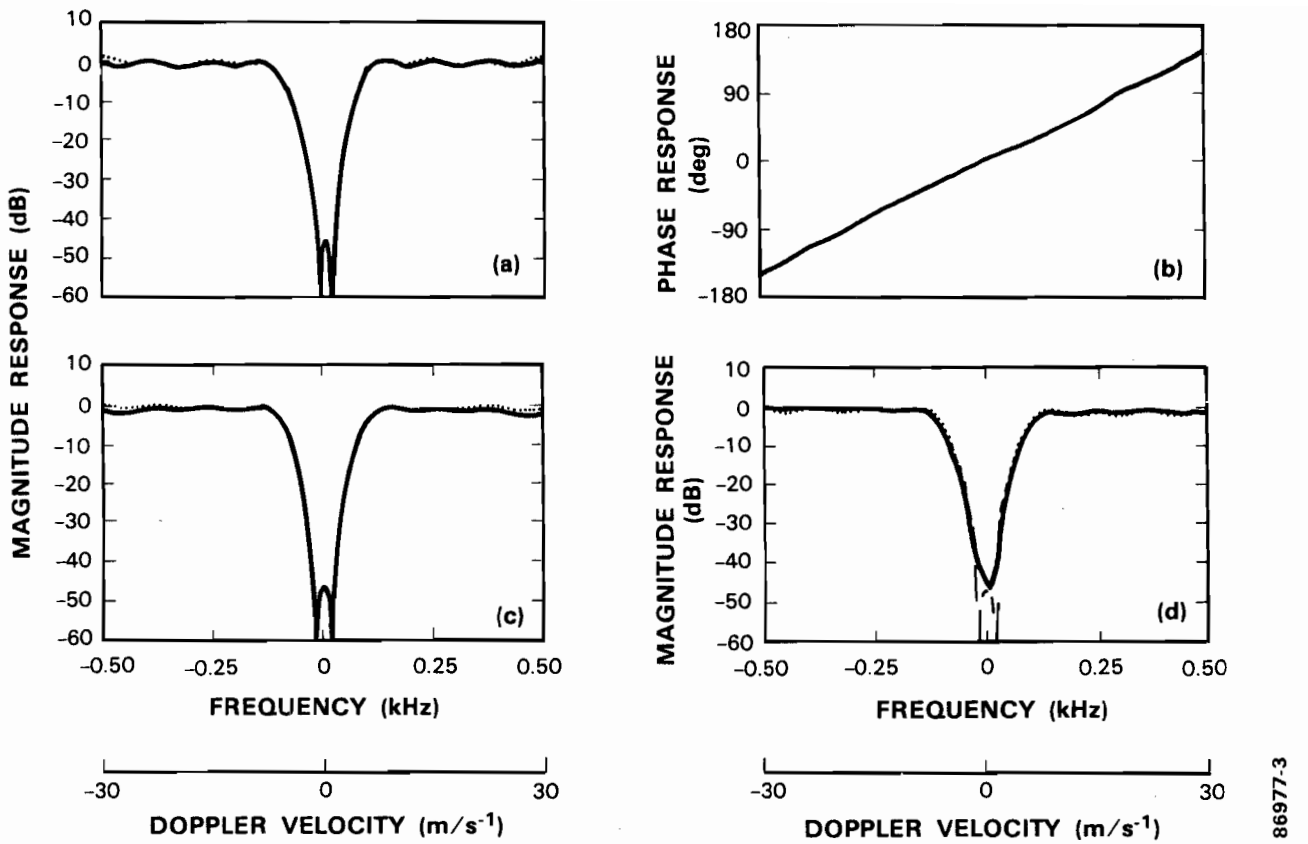

Figure II-3. Clutter filter transfer functions as described in the text. (a) Magnitude response, output point 10; (b) phase response, output point 10; (c) time-averaged magnitude response; (d) time-averaged magnitude response, no interpolation.

the clutter residue levels since these are normalized by the number of data samples at the filter outputs and since the azimuth limits subtended by the extended-CPIs are independent of the number of fill pulses.

D. Clutter-Induced Weather Parameter Estimate Biases and Filter Selection

If the ground clutter residue at a filter output exceeds or is comparable to weather echo power, weather reflectivity estimates will be biased upwards and weather radial velocity estimates will generally be biased towards zero Doppler. Conversely, if "too much" filtering is employed, weather echoes with low radial velocity will be subject to reflectivity underestimates and an upwards bias in estimated mean radial velocity.

Time-averaged magnitude responses for the high-pass filters used for Lincoln testbed ASR signal processing are shown in Figure II-4. These provide ground clutter attenuations ranging from -15 dB to -45 dB with stop-band widths varying from ±2.8 m/s to ±6.1 m/s. The transmitter instability residue for the Lincoln testbed ASR is currently about -45 dB† so that a high-pass filter designed for clutter attenuation in excess of this value would not provide a realizable improvement over the existing design.

Figure II-5 illustrates the trade-offs between weather parameter estimate biases generated by ground clutter residue and those resulting from excessive filtering of the weather echo. For each filter (including the all pass characteristic), the plots show radial velocity and reflectivity bias as a function of true weather velocity. The plots were generated by calculating the (filtered) Doppler spectrum of the weather plus ground clutter; an inverse Fourier transform yields the autocorrelation function from which pulse-pair reflectivity and mean velocity estimates are computed. Figure II-5(a) assumes that the input weather to clutter power ratio is 0 dB and Figure II-5(b) assumes that this ratio is -30 dB. The assumed weather spectrum width, 2.0 m/s, is consistent with measured spectrum widths in low-altitude thunderstorm outflows. The third column in each figure shows the power ratio of weather echo to clutter residue at the filter output. This is closely related to the parameter we use for selecting the "best" filter output -- the measured filter output power over the stored residue map value:

$$R = \frac{WeatherPower + ClutterResidue}{ClutterResidue} = \frac{WeatherPower}{ClutterResidue} + 1 \qquad (5)$$

For simplicity, the ratio "R" in equation (5) will be referred to as simply the "output ratio" in subsequent discussion.

With equal power in the weather and clutter spectrum components (Figure II-5(a)), mean velocity estimates will be approximately midway between the true weather velocity and zero (the ground clutter velocity) when filtering is not employed. Reflectivity estimates are obviously biased upwards by 3 dB. Application of the -15 dB clutter filter increases the filter output weather to clutter ratio to 8 dB or more for all weather velocities. Maximum radial velocity bias is less than 1.5 m/s and reflectivity estimates are accurate unless the weather echo falls within the filter stop-bands. The more attenuating filters result in larger maximum radial velocity biases and a wider region

† Transmitter modifications are under way to reduce the instability residue to less than -60 dB. This will allow for a significant improvement in achievable clutter suppression.

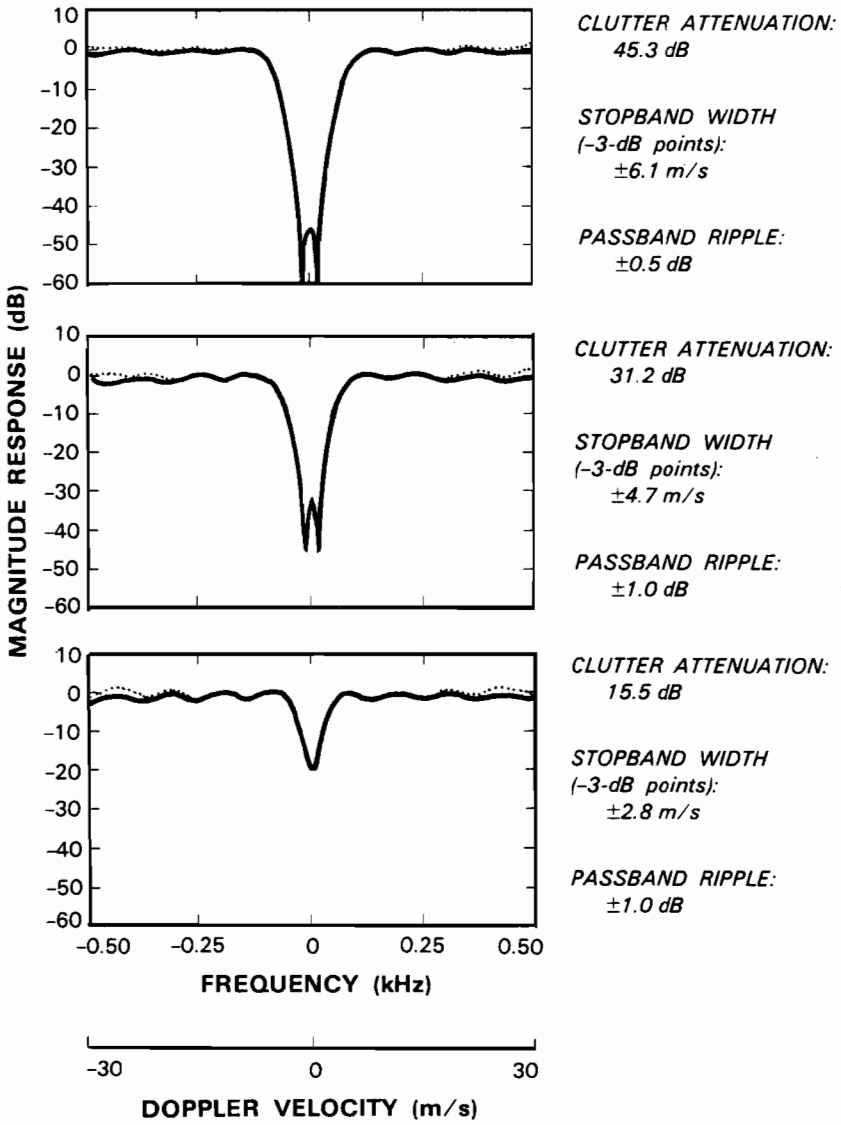

Figure II-4. Time-averaged magnitude responses of the three high-pass clutter filters used for ASR testbed signal processing.

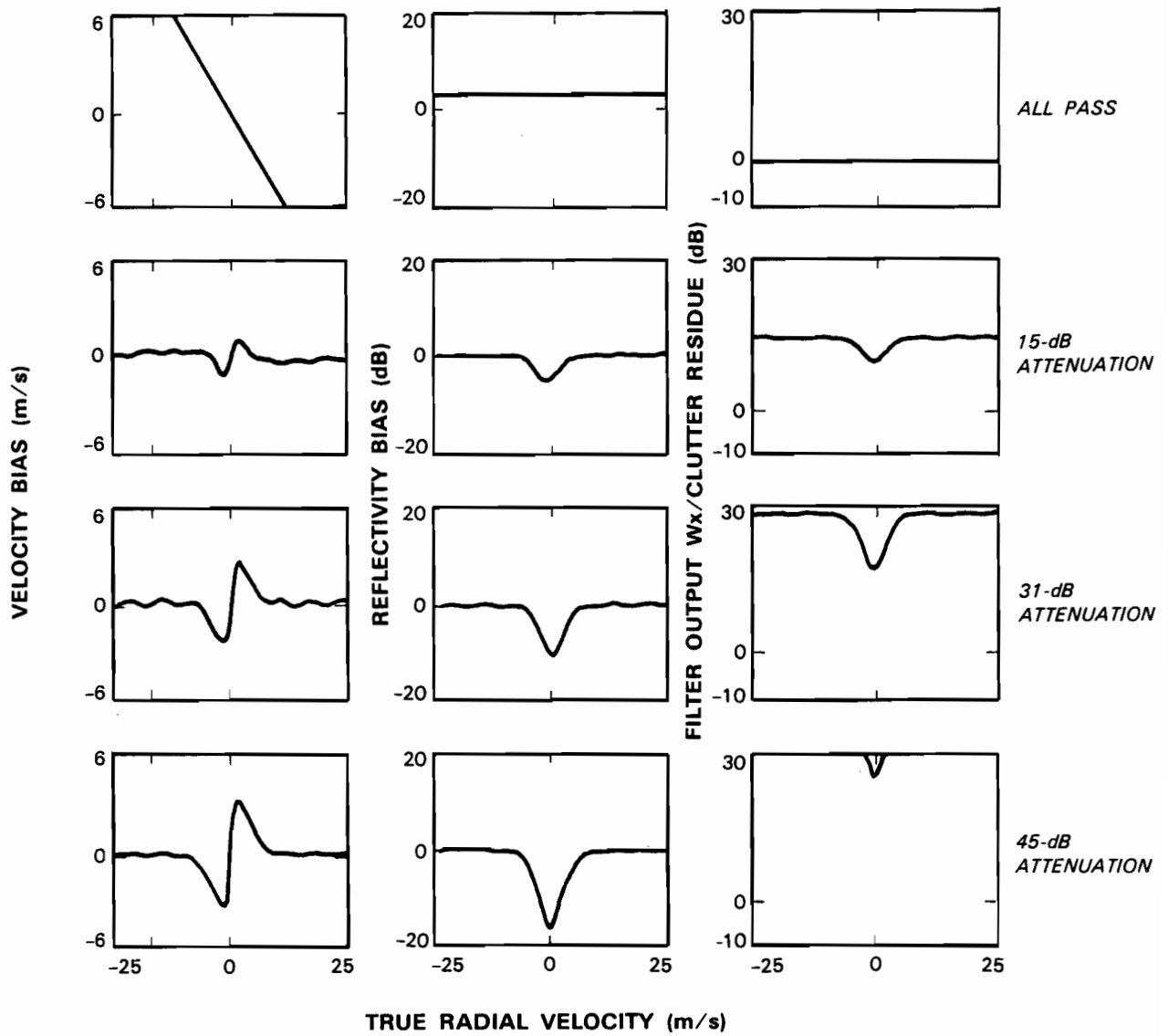

Figure II-5(a). Weather parameter biases and filter output weather to clutter ratio for the all-pass and high-pass filters. The biases are plotted as functions of true weather velocity assuming a weather spectrum width of 2.0 m/s. Assumes Filter Input Weather to Clutter Power Ratio is 0 dB.

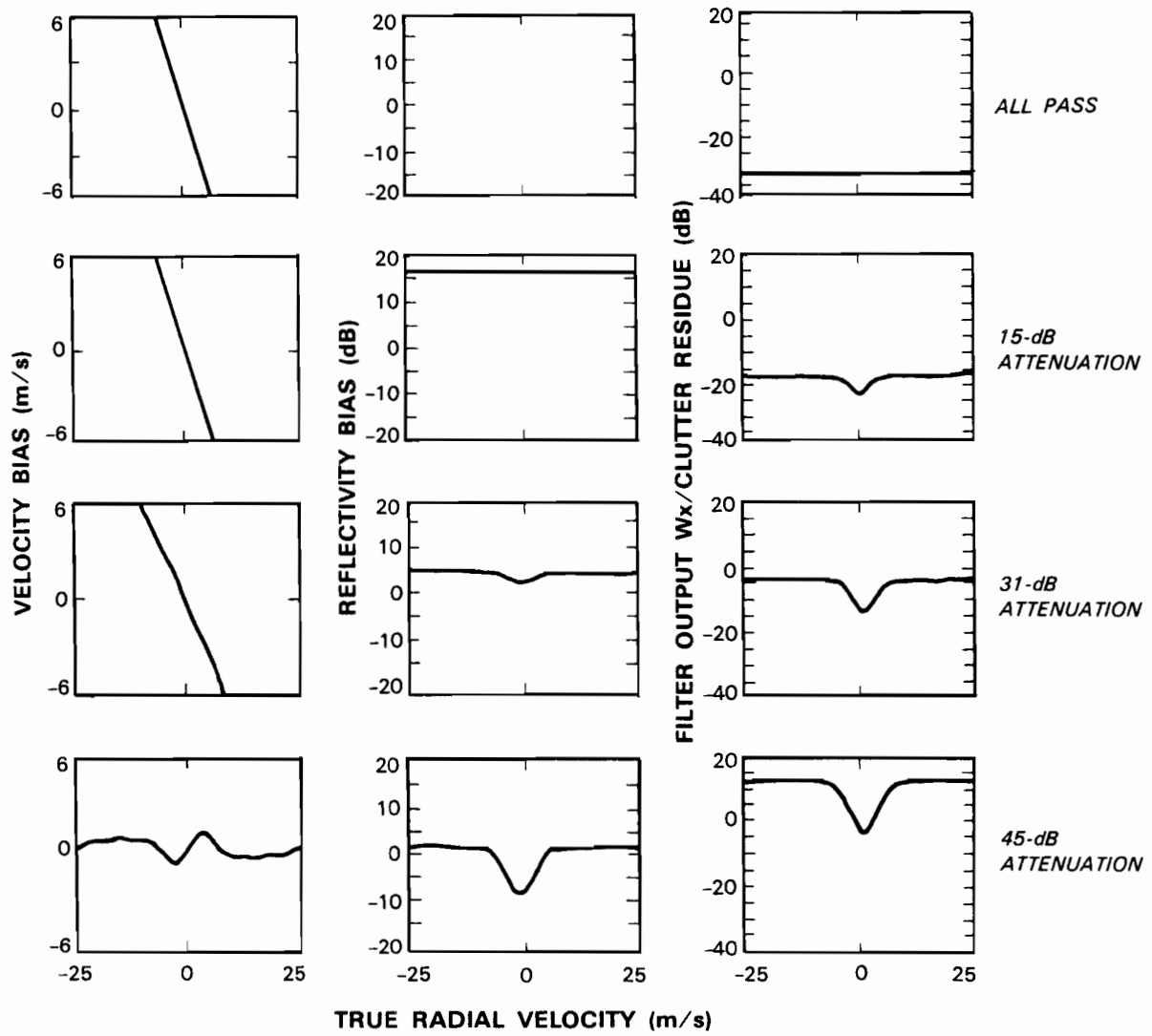

Figure II-5(b). Weather parameter biases and filter output weather to clutter ratio for the all-pass and high-pass filters. The biases are plotted as functions of true weather velocity assuming a weather spectrum width of 2.0 m/s. Assumes filter input weather to clutter power ratio is -30 dB.

around zero Doppler where weather echoes are subject to significant attenuation.

For -30 dB weather to clutter input power (Figure II-5(b)), the most attenuating filter is required to produce weather to clutter ratios at the filter output that are greater than unity. Maximum radial velocity biases (for weather centered in the filter transition bands) are again about 1.5 m/s when this filter is used. Use of the less attenuating filters results in negative weather to clutter ratios and velocity estimates dominated by the low-Doppler clutter residue.

Our signal processing design uses a map of clear-day ground clutter residues to estimate the previously defined filter "output ratio". As can be inferred from Figures II-5, this parameter should correspond to a weather to clutter power ratio that is greater than unity but not excessively so. A simple technique for implementing the filter selection involves testing the estimated output ratios against a threshold (hereafter designated as T_1) and choosing the least attenuating filter that exceeds this threshold for calculation of weather parameters.

The "best" value for T_1 depends on true weather velocity and spectrum width, as well as the input weather to clutter power ratio. Since our selection criterion does not consider these parameters, an appropriate threshold setting can be derived by averaging estimate biases over a range of input weather-to-clutter ratios and over all possible true weather velocities. These average reflectivity and radial velocity estimate biases are shown in Figure II-6(a) as functions of T_1. For each threshold factor, the biases were calculated by:

(1) choosing an input weather to clutter ratio, selecting a filter as described above for each "true" weather velocity, calculating the estimate biases as above, then averaging the absolute value of the estimate biases over true velocity;

(2) repeating this procedure for input weather to clutter ratios of 10 to -40 dB, and averaging over these successive trials.

An alternate performance metric is the peak bias magnitude over possible true weather velocities, again averaged over the range +10 to -40 dB of input weather to clutter ratios. Figure II-6(b) plots this metric as a function of the threshold factor.

The average bias for both reflectivity and radial velocity estimates decreases rapidly as the T_1 is raised from 1 to 6 dB. The average velocity bias is nearly constant for greater threshold factors, whereas average reflectivity bias increases slightly. "Peak" velocity bias also reaches a minimum at a threshold factor setting of 6 dB. In contrast, peak reflectivity bias increases monotonically with the threshold factor; this result reflects the impact on zero-velocity weather of increasingly severe high pass filtering.

Examination of Figures II-6 indicates that an "output ratio" threshold setting of 5 dB -- corresponding to a weather to clutter residue ratio of 3.3 dB -- will produce nearly minimum biases for any of these performance metrics. The resulting radial velocity estimate errors will normally be less than about 2 m/s. Reflectivity biases will be significant only for weather with spectrum components inside the filter stopbands. Maximum reflectivity biases in this situation will be approximately 8 dB.

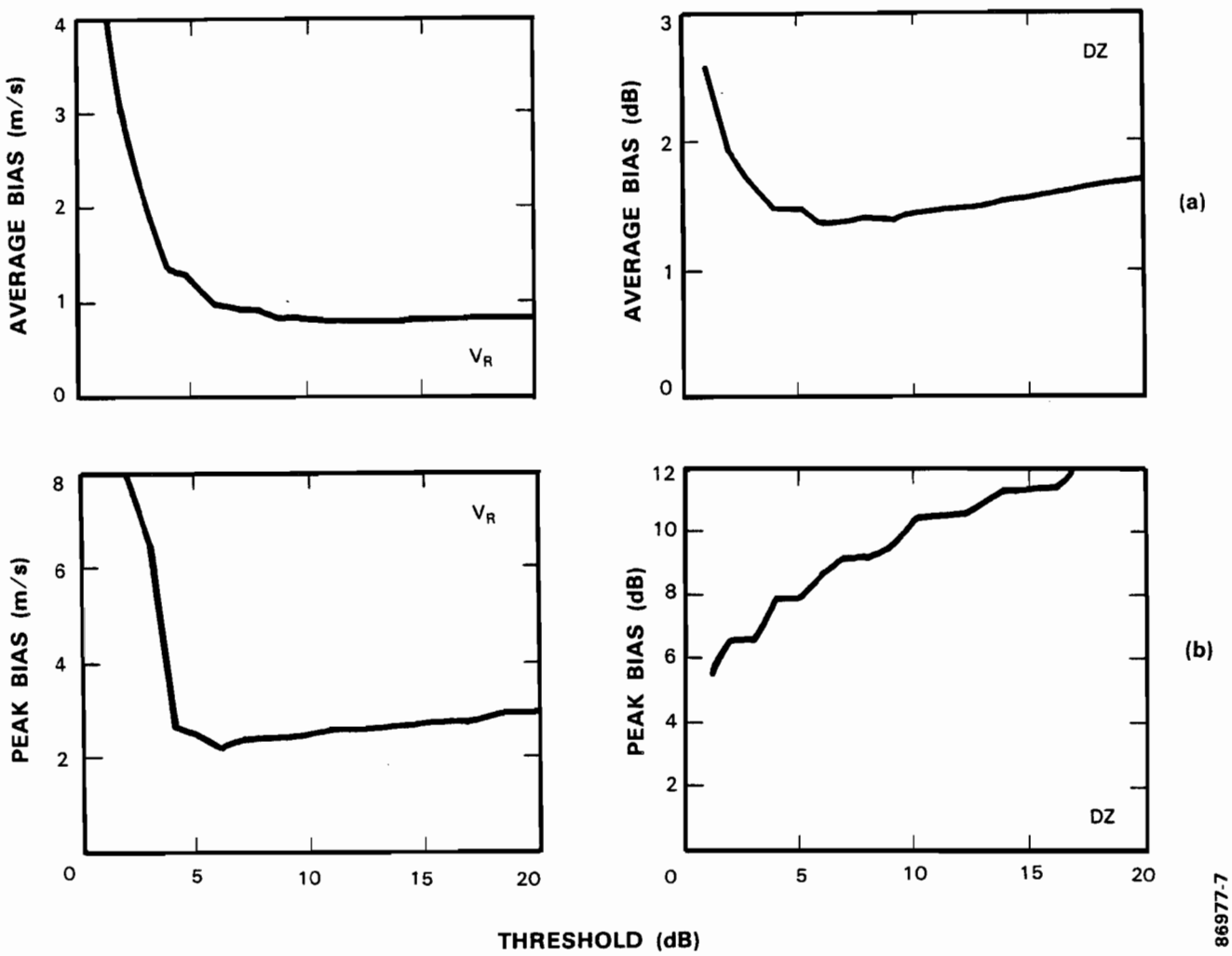

Figure II-6. Radial velocity and reflectivity estimate bias versus "output ratio" threshold setting. (a) Average for input weather echoes spanning a range of weather to clutter power ratios and the Nyquist velocity interval; (b) peak bias (over the Nyquist velocity interval) for input weather echoes spanning a range of weather to clutter power ratios.

III. HUNTSVILLE GROUND CLUTTER MEASUREMENTS

A. Spatial Distribution

Figures III-1 is a map of the area around Lincoln Laboratory's testbed ASR in Huntsville, Alabama. As can be seen, terrain around the radar is undulating with local relief of roughly ±5 m. The ground generally rises towards the north and east, reaching a local maximum at Rainbow Mountain (150 m above the radar site) at 11 km range, 40° azimuth. The terrain falls off by about 15 m to the south and west towards the Tennessee river (10 km range at its closest point). The area is generally lightly settled, consisting of plowed fields, lines of trees serving as windbreaks and isolated houses. Exceptions are:

(1) the Huntsville airport complex (east to southeast at 3 km range);

(2) the town of Madison (northeast at 7 km range);

(3) forested wildlife refuges to the west and southwest (2 to 5 km range) and to the east at ranges greater than 10 km. The clutter measurements reported here were obtained during spring and summer (April-July 1987) so that the deciduous trees were fully leaved;

(4) Alabama State Highway 20, running from west-southwest to east-northeast and passing within 500 m of the radar.

Figure III-2(a) is a PPI display of ground clutter cross section densities, σ_0 (m^2/m^2), measured with the low beam of the testbed ASR. The same data are shown in III-2(b), scaled to an equivalent weather reflectivity factor (dBz). The displays extend only to 12 km range since this is the area of primary operational interest for low altitude wind measurements [7]. Sources of significant clutter at this site are topography (Rainbow, Weeden and Mackin Mountains to the northeast), man-made structures (power lines, buildings at Huntsville airport and in the town of Madison), auto traffic on Highway 20, and forested areas such as that immediately west of the radar. Median clutter reflectivities (ensembled over all azimuths) are -43 dB (44 dBz) at 1 km and -49 dB (32 dBz) at 10 km. These values are representative of clutter intensity measurements we have made using operational ASRs at major air terminals [1].

The boxes overlaid on the images indicate small spatial areas where subsequent analysis will focus: the leading slope of Rainbow Mountain, Huntsville Airport, the forested wildlife refuge immediately west of the radar and trees and farmland along Limestone Creek to the northwest of the site. These spatial patches return moderate to intense ground clutter echoes and were chosen as representative of the sources of clutter that are important at this site. Table III-1 summarizes the distribution of clutter intensity levels for each area. Listed are the median, 10^{th} and 90^{th} percentile of the clutter cross section density σ_0 and equivalent weather reflectivity factor probability distributions.

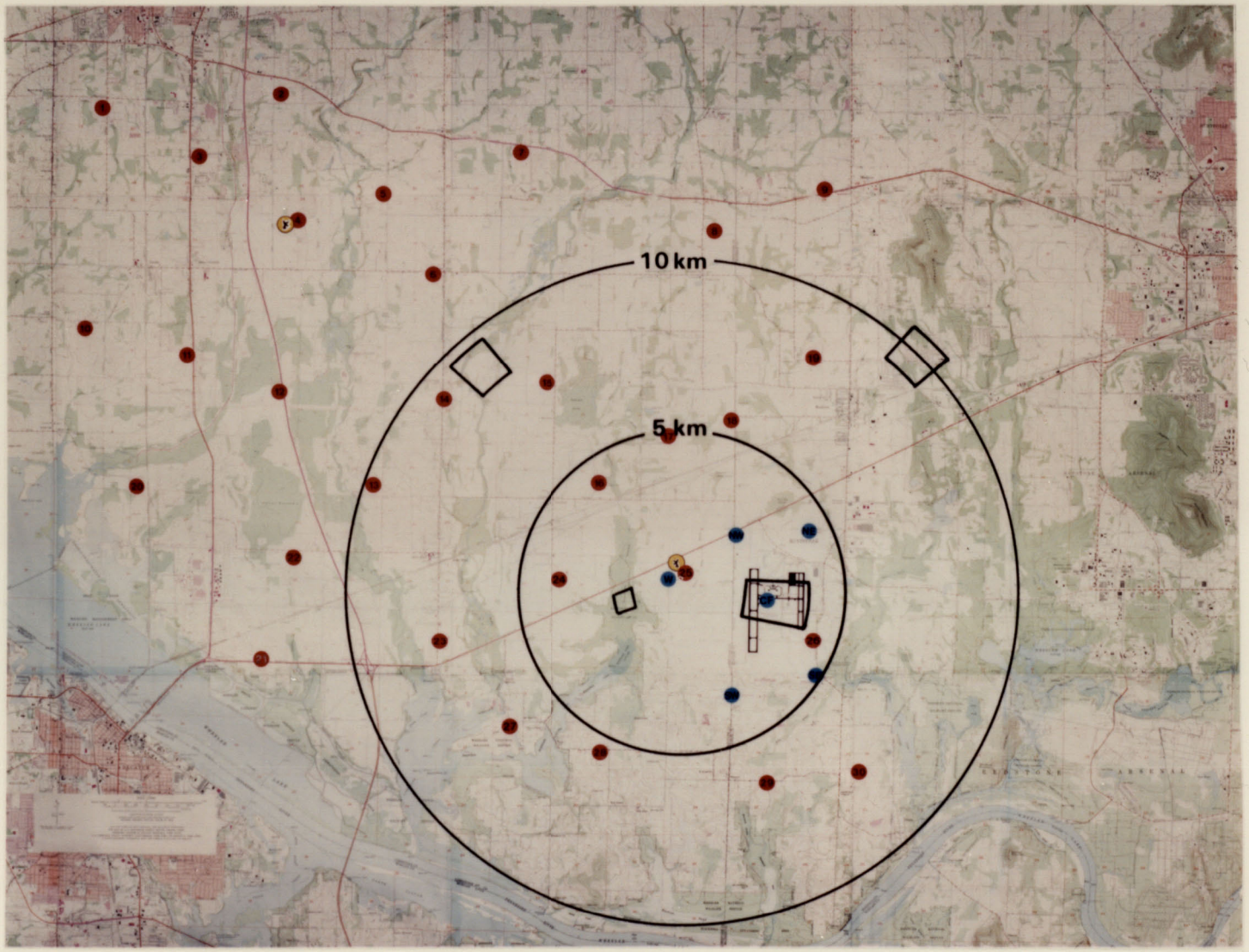

Figure III-1. Map of the area around Lincoln Laboratory's testbed ASR near Huntsville, Alabama.

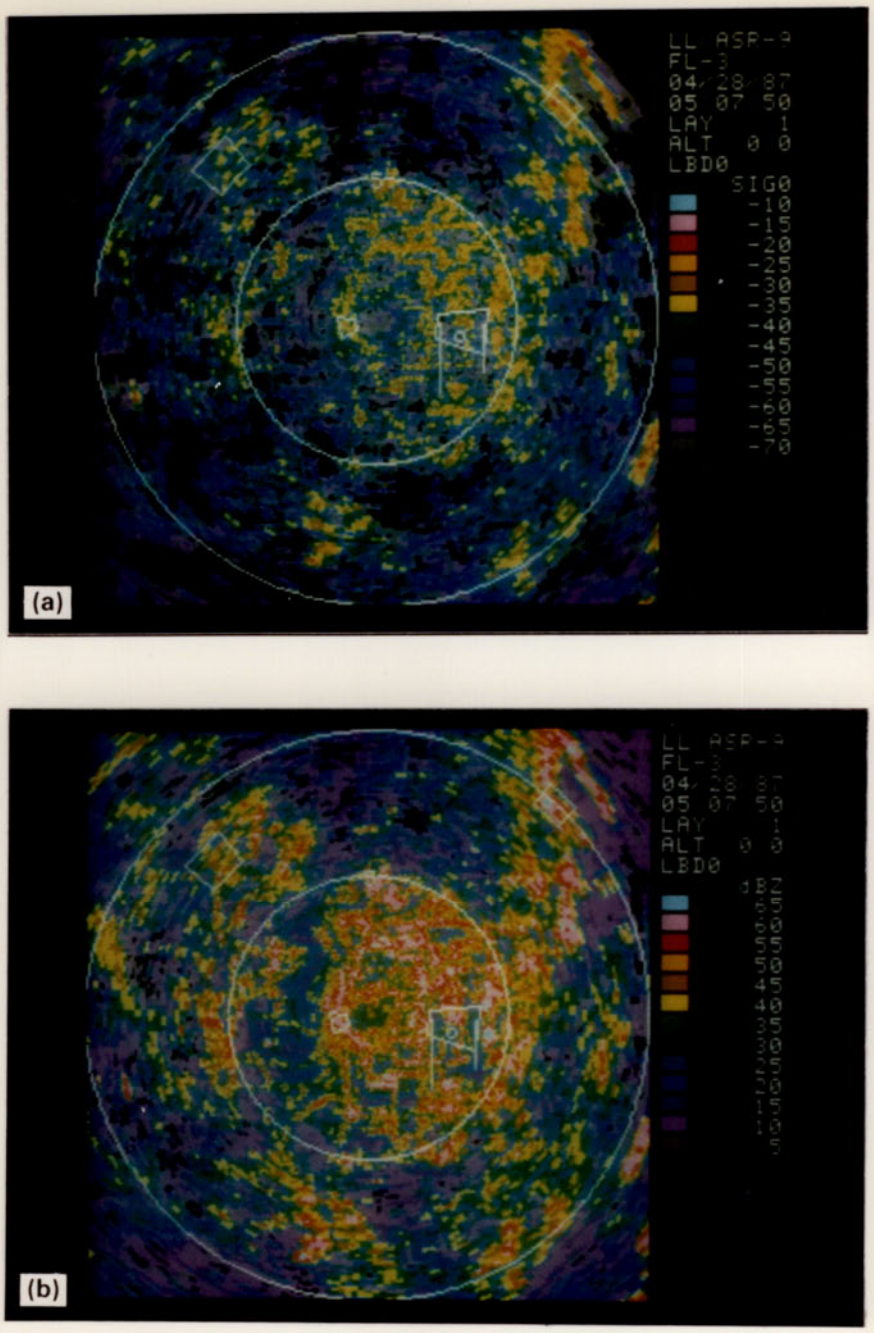

Figure III-2. (a) Display of ground clutter cross section density σ_0 from the testbed ASR. The white boxes show areas for analysis of clutter intensity fluctuations: (1) Rainbow Mountain (northeast at 10 km); (2) Huntsville Airport (east at 3 km); (3) Wildlife Refuge (west at 1.5 km); (4) Limestone Creek area (northwest at 8 km); North-south oriented parallel lines indicate the runways at Huntsville Airport; (b) display of the equivalent weather reflectivity factor of ground clutter from the testbed ASR.

Table III-1: Summary of Ground Clutter Distributions						
	σ_0 (dB)			dBz		
Area	10%	50%	90%	10%	50%	90%
Rainbow Mt.	-52	-27	-21	36	55	59
Airport	-58	-43	-28	22	35	59
Forest	-47	-34	-30	32	57	63
Limestone Creek Area	-54	-40	-31	24	42	51

In each of the patches, the median ground clutter intensity corresponds to moderate (35 dBz) to heavy (>50 dBz) precipitation. Thus extensive use of the high pass clutter filters will often be required in these areas to achieve positive weather to clutter power ratios.

B. Temporal Variation of Clutter Intensity

The filter selection procedure described in Section II(c) presumes that the stored clutter residue map can be used to accurately calculate the decision parameter, the filter "output ratio". This residue map is generated by averaging many scans of ground clutter measurements on a cloud free day to form an estimate of the mean ground clutter intensity in each resolution cell. We currently update the clear day measurements at two week intervals.

A single realization of the clutter intensity field will differ from the average of many scans owing to movement -- on the order of the radar wavelength -- of the individual scatterers in each resolution cell. We expect that such movement takes place on a time-scale long compared to the 0.026 s CPI length but short compared to the interscan period (4.8 s). Billingsley and Larrabee [8] report a 0.081 second e-folding time for the normalized autocorrelation function of S-band radar returns from trees on a windy day. In general, a resolution cell will also contain scatterers (buildings, bare slopes) that do not move significantly from scan-to-scan. Thus, scan-to-scan fluctuations of the CPI-averaged clutter intensity level in a resolution cell can be modeled with a non-central Gamma density function [9]:

$$p(x)=\frac{1}{2\sigma^2}\left(\frac{x}{\lambda}\right)^{\frac{M-1}{2}}\exp\left[\frac{-x-\lambda}{2\sigma^2}\right] I_{M-1}\left(\frac{\sqrt{x\lambda}}{\sigma^2}\right) \qquad (6)$$

Here M, the number of independent samples in a CPI is taken as equal to unity owing to the above assumption on decorrelation time. $I_{M-1}(z)$ is the modified Bessel function of the first kind, order $M-1$. The RMS power of the temporally fluctuating echo component is σ. For M equals 1, the non-central parameter λ is simply twice the power ratio of the temporally stable echo component to the fluctuating component. When M equals 1 and the non-central parameter is zero (i.e. there is no stable echo component), the density function reduces to the exponential function.

Figure III-3 plots the measured probability distribution of single-scan clutter intensity fluctuations for each of the spatial patches identified above. When the measurements were made, wind speed was 5 m/s from 350°. The abscissa is the ratio of single-scan intensity to the average of 100 scans. The smooth curves fit non-central Gamma density functions to the data, using the indicated non-central

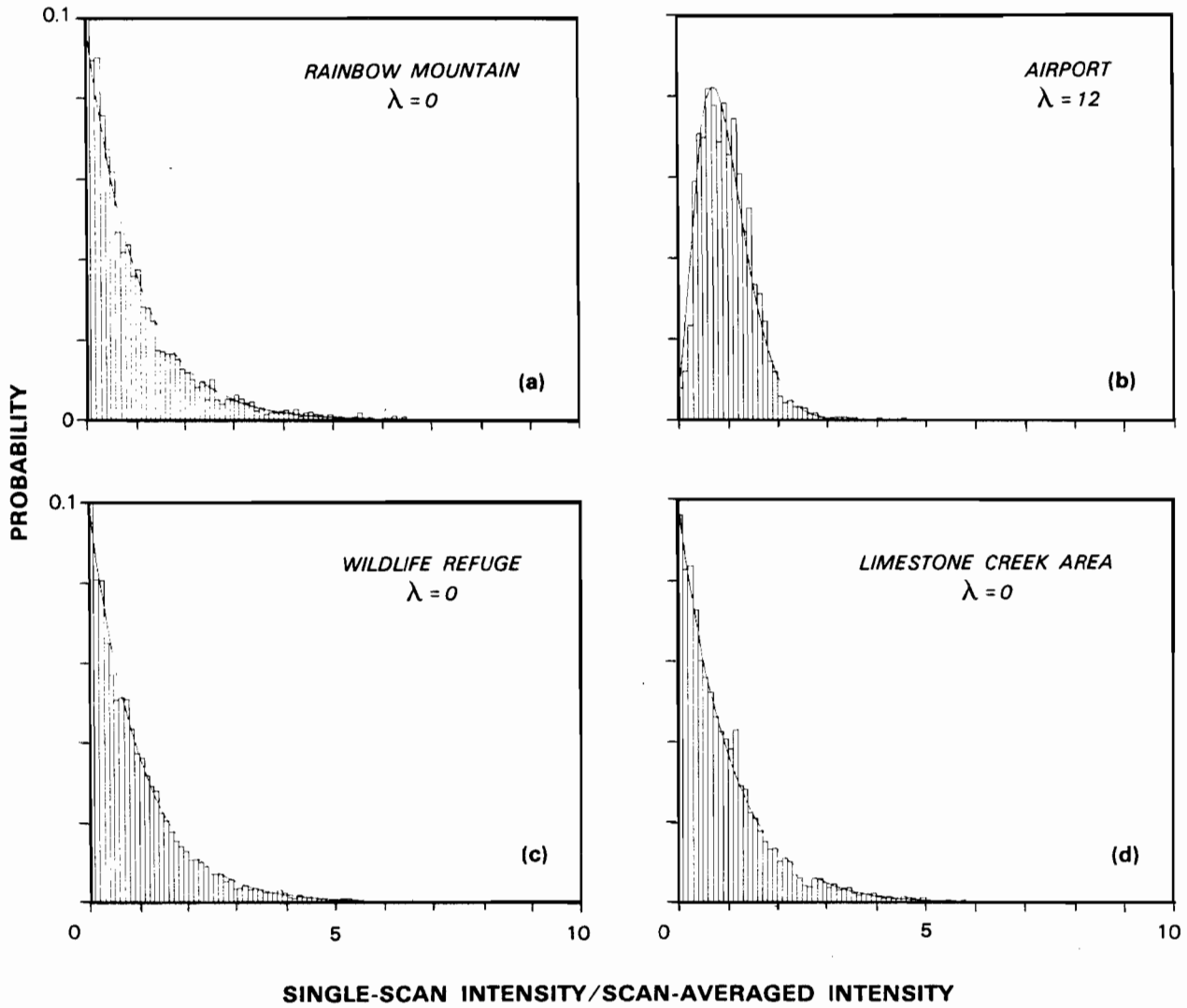

Figure III-3. Histograms showing the distribution of scan-to-scan clutter intensity fluctuations. Abscissa is the ratio of single scan, CPI-averaged clutter power to the average of 100 scans in the same resolution cell. Parts (a)-(d) are for different spatial patches as described in the text. The smooth curves are non-central gamma density functions with the indicated parameters.

parameters. Note that these analytic density functions have been multiplied by the histogram bin width (0.1) to make the ordinates match the measured probabilities.

In three of the four patches, the stable echo component is negligible and the measured distributions are nearly exponential. This is consistent with the supposition that the dominant scatterers in each of these mainly undeveloped patches were windblown trees and shrubs. In contrast, the airport patch contains buildings as well as flat grassy and paved surfaces along the runways (note the correspondingly low scattering cross sections in Figure III-2). In this patch, the best fit non-central Gamma function implies that the stable echo component is six times more intense than the fluctuating component. If the distributions from the four areas are combined, the cumulative distribution reaches 0.99 when the single-scan to scan-averaged power ratio is 5.

Another source of discrepancy between the stored clutter residue map and actual clutter intensity is long-term variation of the scan-averaged clutter intensity in a resolution cell. This may occur owing to changes in natural ground cover (e.g. trees leafing out), human effects (construction, movement of vehicles) or variation of RF propagation paths owing to atmospheric temperature structure. While we do not make ground clutter measurements frequently enough to define the temporal progression of such long-term variations, we can perform a practical measurement of the magnitude of the variations by comparing clutter data obtained on two different days separated by two weeks. Since this is the update interval for our clutter residue map, the measured variability will accurately define the impact of long-term clutter intensity changes on the signal processing algorithms.

Figures III-4(a)-(d) histogram these two-week intensity changes for resolution cells within the spatial patches described previously. Owing to the relatively small number of resolution cells in the patches, these histograms do not clearly define the underlying distribution of long-term clutter intensity changes. Thus, in Figure III-4(e) we include all resolution cells within 12 km of the radar. Overall, long-term variations in the mean clutter intensity level in a resolution cell are of comparable magnitude to the scan-to-scan fluctuations discussed previously.

Our signal processor uses scan-averaged clutter residue values that may be as much as two weeks old to estimate the output ratio applying to a single realization of ground clutter echoes. Thus variability on both of the time scales considered above contributes to errors in the estimate. The density function describing the composite single-scan to residue map clutter variability is:

$$p_z(z) = \int_0^\infty p_y(y) p_x(\tfrac{z}{y}) dy \qquad (7)$$

Here $p_y(y)$ is the density function describing long-term clutter intensity changes and $p_x(x)$ describes the scan-to-scan fluctuation. Figure III-5(a) shows the composite density function of equation (7) using the spatially averaged measurements from Figure III-4(e) and a combination of the density functions shown in Figure III-3. The cumulative distribution is shown in part (b).

The resulting distribution has a considerably larger "tail" than either of the contributing short- or long-term fluctuation distributions. For z greater than 3.0, the density function is significantly greater than exponential. The probability that the single-scan clutter intensity exceeds the clutter map value by more than a factor T_2 does not drop below one percent until T_2 is 8.

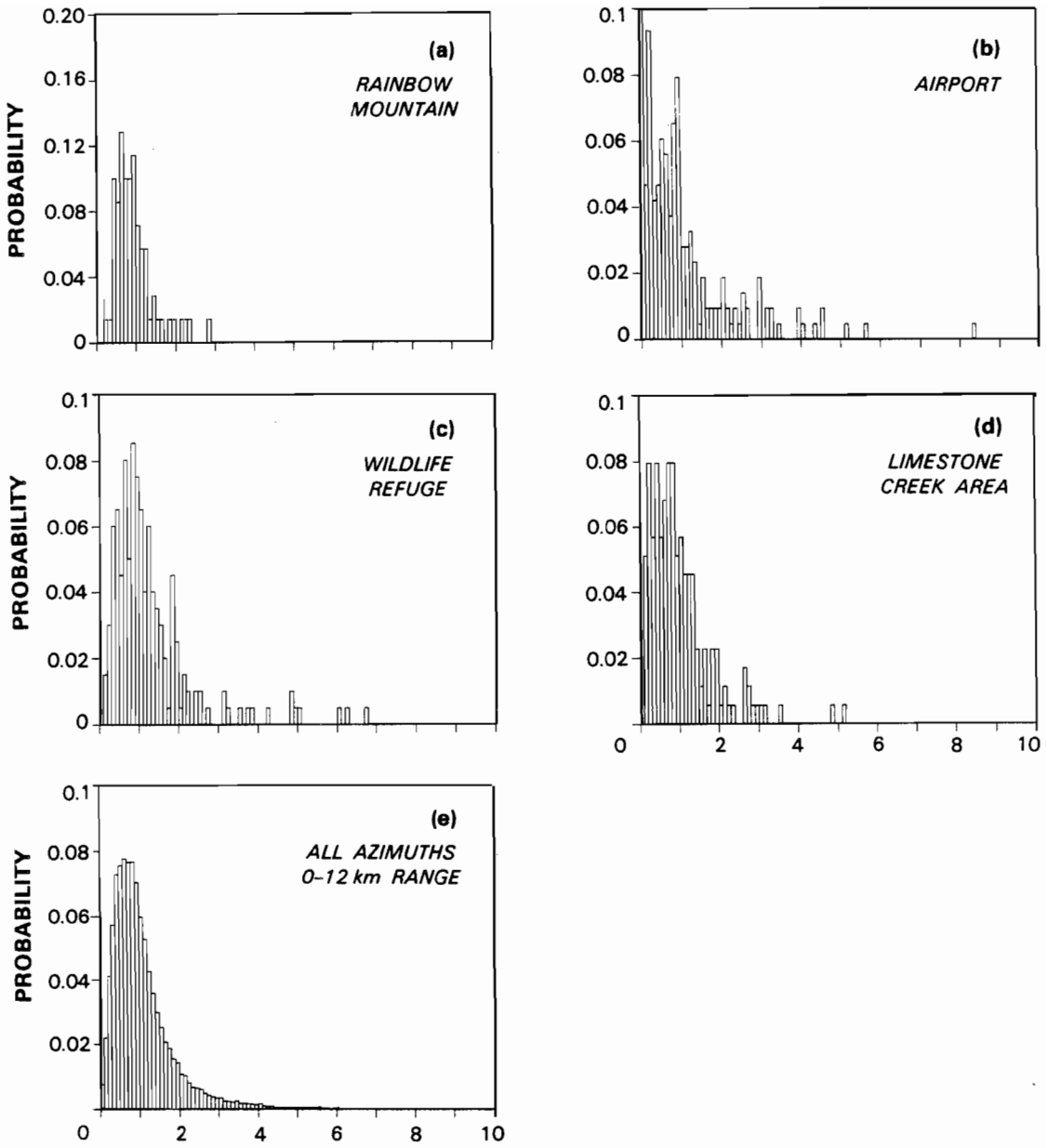

Figure III-4. Histograms showing the distribution of long-term fluctuations of scan-averaged clutter intensity within a resolution cell. The distributions were generated by comparing scan-averaged clutter measurements on two clear days separated by two weeks. Parts (a)-(d) are for the different spatial patches described previously. Part (e) treats all resolution cells within 12 km of the testbed ASR.

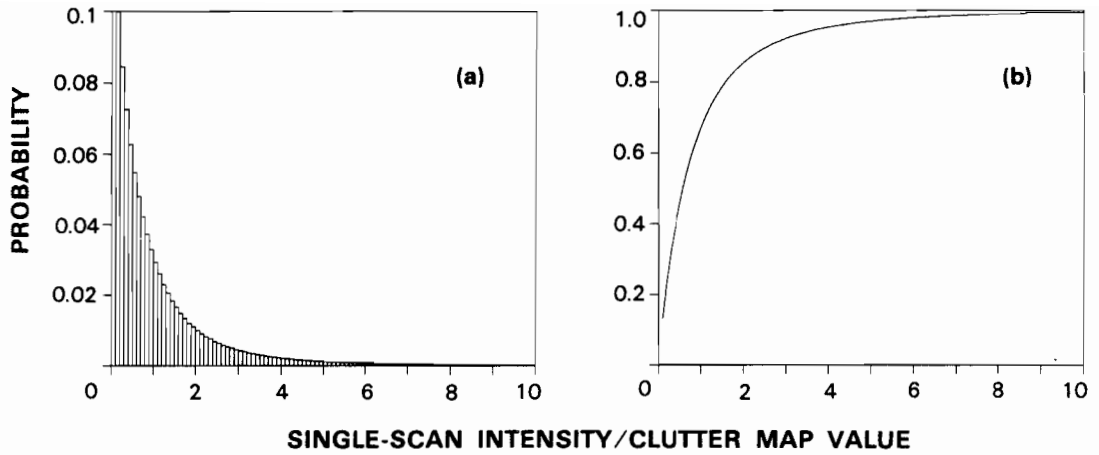

86977-13

Figure III-5. Composite clutter fluctuation distributions. Data from Figures III-3 and III-4 are combined (Equation 7 in the text) to compute the distribution of single-scan clutter intensity to a scan-averaged value measured as much as two weeks earlier. (a) Probability density function; (b) cumulative distribution.

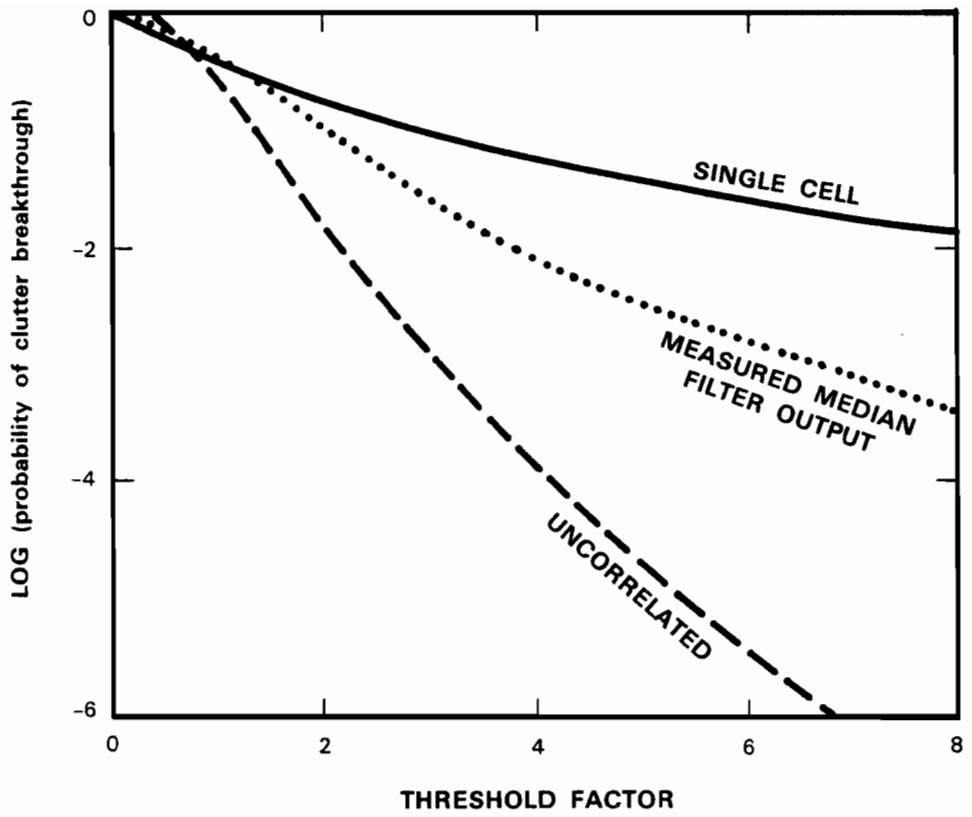

Figure III-6. Clutter breakthrough probability versus threshold setting T_2 (see text). The upper curve assumes no spatial filtering. The lower curve includes the effect of the spatial median filtering, assuming that intensity fluctuations over the filter window are statistically independent. The middle curve shows the effect of spatial median filtering when intensity fluctuations within the filter window are partially correlated.

We will define "clutter breakthrough" as occurring when the actual filter output ratio is less than the threshold T_1 defined in Section II(c) at the same time that the estimated output ratio exceeds T_1. In this situation, a less attenuating filter than required would be chosen, possibly resulting in large reflectivity and radial velocity estimate biases as illustrated in Section II. To prevent breakthrough, the output ratio threshold must be increased to:

$$T_3 = T_1 T_2 \tag{8}$$

where T_2 accommodates clutter intensity variations. To simplify subsequent analysis we set the weather power equal to zero; the breakthrough probability as a function of T_2 is then simply one minus the cumulative distribution in Figure III-5(b).

We allow for one occurrence of clutter breakthrough per azimuth sector inside the 12 km range radius where low-altitude wind measurements are operationally important. This translates to a one-percent probability of breakthrough.

C. Spatial Correlation of Clutter Intensity Fluctuations

As stated above, to maintain the clutter breakthrough probability at less than one percent the threshold T_3 must be increased by a factor of 8 relative to the optimum setting derived in Section II(c). The median ratio of single-scan clutter power to the value stored in the clutter map is unity however (see Figure III-5(b)). Thus, in the majority of resolution cells, the actual output ratio will be well above the optimum ratio when the threshold T_3 is used. Although this would not greatly increase radial velocity estimate bias it would significantly increase reflectivity biases for low radial velocity weather owing to more severe clutter filtering (see Figure II-6) .

To reduce the need for "over-filtering", we use a spatial median filter at the output of the signal processor's pulse-pair estimator. This operates on each resolution cell and its eight nearest neighbors under the assumption that clutter breakthrough will not occur simultaneously over the majority of cells in the cluster. If we assume that clutter intensity fluctuations for different cells within this cluster are statistically independent, then the breakthrough probability at the median filter output, $p_b(out)$, is related to the single-cell breakthrough probability, $p_b(in)$, by:

$$p_b(out) = \sum_{m=5}^{9} p_b(in)^m [1-p_b(in)]^{9-m} \frac{9!}{m!(9-m)!} \tag{9}$$

The solid and dashed curves in Figure III-6 plot respectively the measured single-cell breakthrough probability and the predicted (from Equation (9)) median filter output breakthrough probability as a function of the threshold factor T_2.

In reality, clutter intensity fluctuations in adjacent resolution cells will not completely decorrelate owing to the radar's azimuth or range sidelobes, and range or beam "splitting" of discrete scatterers. Figure III-7 plots the distribution of spatial cross-correlation coefficients for all 9-cell, nearest-neighbor clusters within 12 km of the Lincoln testbed ASR. We define this cross-correlation coefficient for each cluster as the average of the off-diagonal terms of the covariance matrix:

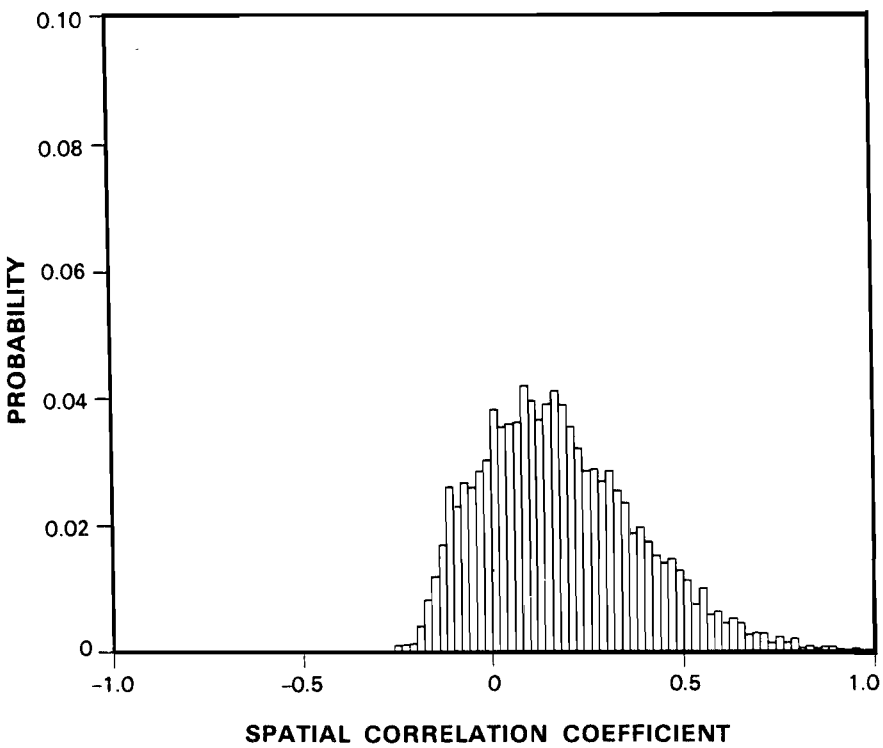

86977-15

Figure III-7. Distribution of cross-correlation coefficients for intensity fluctuations in resolution cells within the spatial filter window. This histogram is from all 9-cell nearest neighbor clusters within 12 km of the testbed ASR.

$$C = \frac{<(x_i - <x>)(x_j - <x>)>}{\sqrt{<(x_i - <x>)^2>}\sqrt{<(x_j - <x>)^2>}} \tag{10}$$

$$= \frac{2}{9-1} \frac{\sum_{i=1}^{9} \sum_{j=i+1}^{9} (x_i - <x>)(x_j - <x>)}{\sum_{i=1}^{9} (x_i - <x>)^2}$$

Here, i and j index the 9 cells within a spatial cluster and the x_i are measured ratios of single-scan clutter intensity to scan-averaged clutter intensity two weeks earlier. $<x>$ is the (global) mean of the x_i.

The measurements indicate a weak positive correlation between intensity fluctuations in adjacent resolution cells. The median of the distribution in Figure III-7 is 0.15. This partial correlation among cells in the median filter cluster requires substitution of conditional distribution functions in the relation between $p_b(out)$ and $p_b(in)$. The dotted curve in Figure III-6, a direct measurement of the clutter breakthrough probability at the median filter output, shows the effect of the partial correlation of intensity fluctuations within the cluster. If clutter intensity fluctuations were independent from cell to cell, the threshold factor T_2 could be set at 2.1 to produce the required one-percent breakthrough probability at the median filter output. Because of intra-cluster correlation, this threshold must be raised to 4. This still represents a significant improvement relative to the setting -- eight -- that would be required if spatial filtering were not employed.

In summary then, the filter selection procedure involves testing the ratio of measured filter output power to the stored clutter map value against a threshold. This threshold is currently set to 11 dB in accordance with equation (8) and the arguments presented in Sections II(c) and III(c). The least attenuating filter output that satisfies the threshold criterion is then used to estimate the weather parameters.

The scan period of an ASR is short relative to the time scale for significant evolution of weather reflectivity or radial velocity fields. Thus, the effect of temporal fluctuations in ground clutter intensity could be further reduced by cell-averaging each filter's output power over successive antenna scans before making a decision on which filter to employ. We have chosen, however, to process on a single-scan basis since:

(1) the clutter breakthrough probability is already acceptably low;

(2) the high update rate provided using single scan measurements may facilitate automatic wind-shear detection.

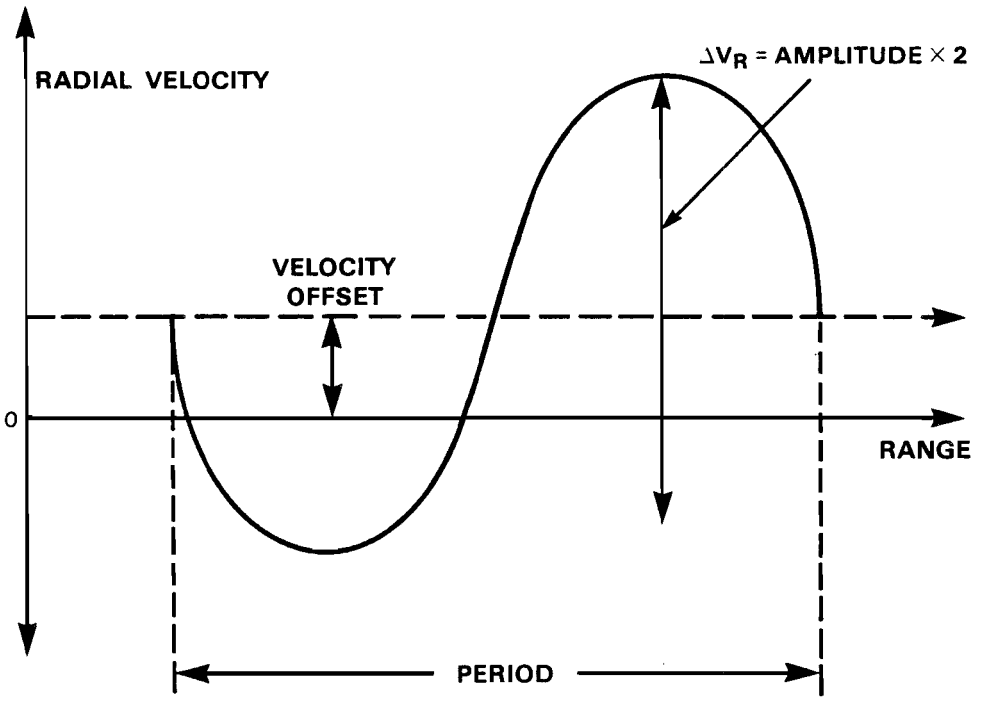

Figure IV-1. A simple model for radial velocity versus range in a microburst.

IV. EVALUATION OF CLUTTER PROCESSING PERFORMANCE

In sections II and III, we defined a signal processing architecture and showed how the temporal and spatial properties of ground clutter dictate the setting of processor parameters. We next evaluate the performance of our processing algorithms using measured Huntsville ground clutter and simulated or measured weather signals. Our evaluation with simulated weather signals (Section IV-A) will concentrate on the accuracy of radial velocity measurements rather than reflectivity measurements since:

(a) radial velocity is the primary data source for detection of low-altitude wind shear regions;

(b) thunderstorm precipitation cores (i.e. reflectivity structures) have much greater vertical extent than the divergent outflow winds that they generate. Thus, at short range where wind shear detection is operationally significant, the high receiving beam will provide reflectivity measurements that are as reliable as low beam data. Reference [3] treats in detail the impact of ASR ground clutter on weather reflectivity factor measurements.

The real weather data presented in Section IV-B provide comparisons of reflectivity factor measurements from the ASR testbed and collocated meteorological radars.

A. Simulated Weather

Figure IV-1 shows a simple model for radial velocity versus range in a microburst. The "signature" is taken as one cycle of an inverted sine wave, parameterized by its amplitude (one-half the magnitude of the velocity differential across the event), a velocity offset (the parent storm's mean translational velocity) and its period (the horizontal dimensions of the wind shear region). An assumed radar reflectivity factor and velocity spectrum variance complete the model.

This model is used to compute the weather echo power spectrum at each sampling gate along the "microburst". As indicated in Figure IV-2, these spectra are summed with corresponding ground clutter spectra derived from single-scan clutter measurements from our testbed ASR. The composite spectra are then "filtered" using each of the transfer functions in Figure II-4 (and an all-pass characteristic). "Output ratios" (equation 5) are computed from the filtered spectra and a scan-averaged clutter residue map. Note that the residue map is derived from measurements preceding the single-scan data by two-weeks so that the impact of ground clutter intensity fluctuations is accurately simulated. Filter selection, pulse-pair reflectivity/radial velocity estimation and spatial smoothing are then performed as described previously.

We quantify the effect of ground clutter on ASR wind measurements using the normalized cross-correlation coefficient between the calculated output radial velocity versus range signature and the input model. This performance metric defines the degree to which the shear signature would be distorted by ground clutter and the requisite clutter filtering; it is thus a reasonable indicator of the impact of ground clutter on a post signal-processor "detection" algorithm which seeks to automatically identify hazardous shear regions. We declare the velocity measurements to be acceptable when this cross-correlation coefficient exceeds 0.9. Figure IV-3 shows examples of calculated "microburst signatures" that pass and fail this acceptance criterion.

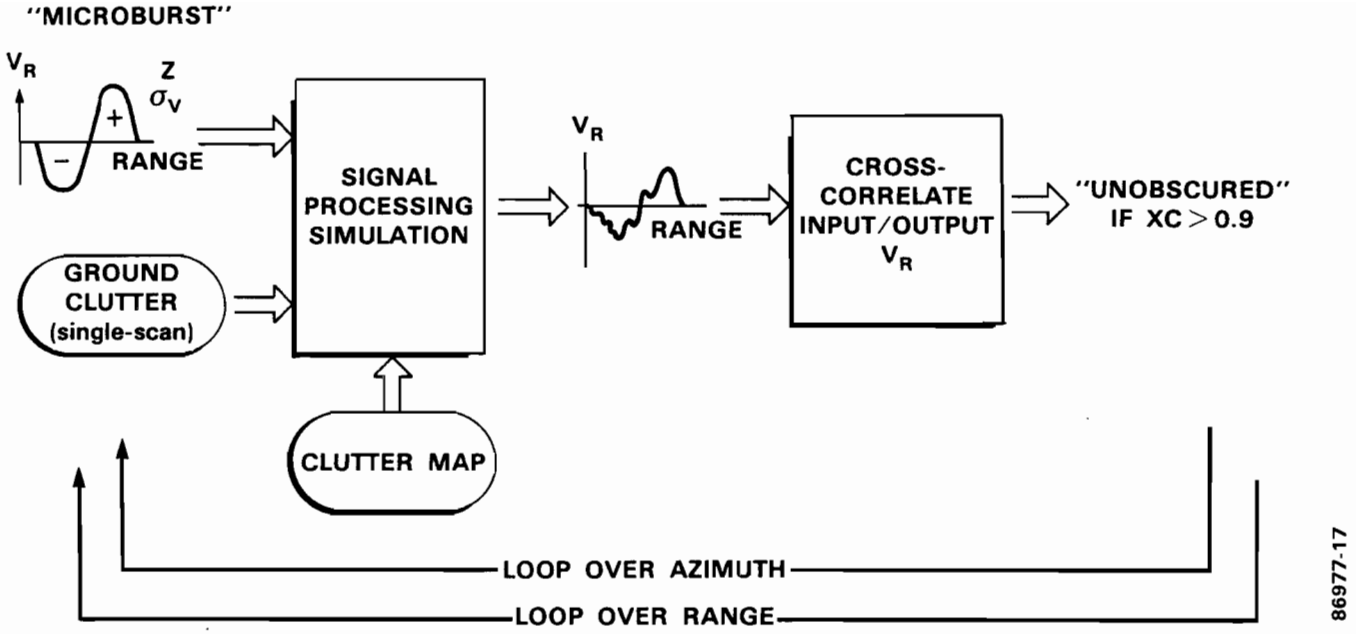

Figure IV-2. Block diagram of the procedure used for calculating areas of "obscuration" caused by ground clutter or clutter filtering.

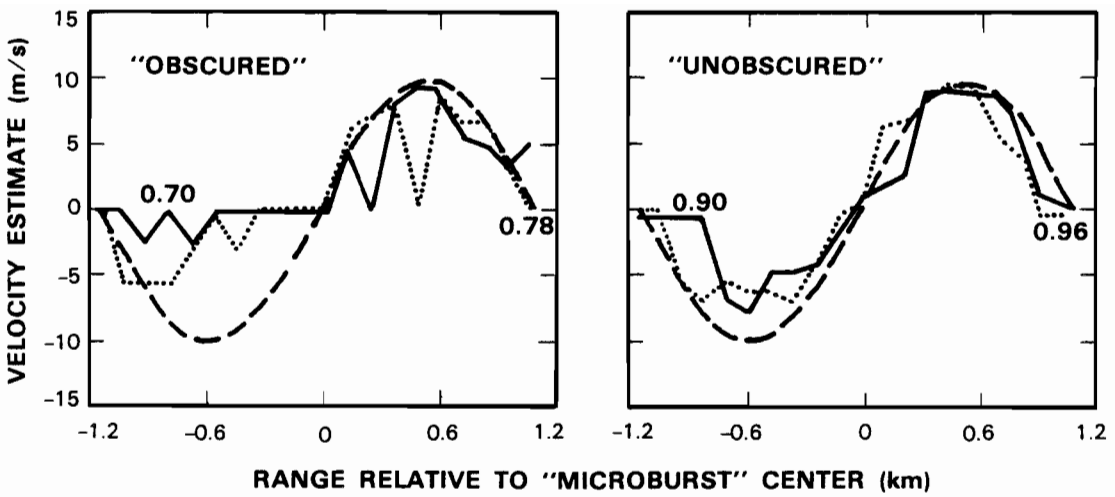

86977-18

Figure IV-3. Examples of simulated processor output "microburst" signatures that pass and fail the obscuration test described in the text. The dashed lines show the input signature. Labels on the other curves give the normalized cross-correlation coefficient between the input and output signatures.

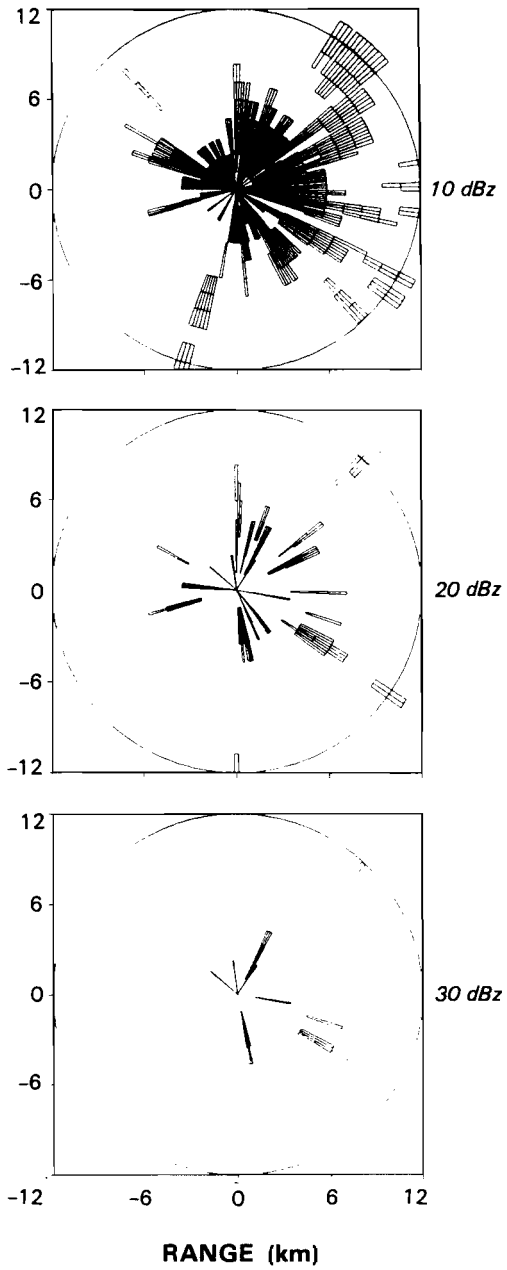

86977-19

Figure IV-4. Areas of obscuration for a microburst with velocity differential of 20 m/s, no velocity offset and 2.4 km radial extent. Weather reflectivity factors of 10, 20 and 30 dBz are assumed.

By moving the model shear signature over range and azimuth, we define the areas where ground clutter at the Huntsville site would prevent reliable detection of low altitude wind shear. As previously, we will assume that weather spectrum width is 2.0 m/s.

Figure IV-4 maps the regions of ground clutter obscuration for assumed weather reflectivity factors of 10, 20, and 30 dBz. For these calculations we have set the amplitude of the shear signature to 10 m/s (20 m/s total shear) with no velocity offset. The range extent of the "microburst" signature is taken as 2.4 km.

When the weather reflectivity factor is 10 dBz or less, the clutter residue in resolution cells at close range will often be of comparable or greater magnitude, even when the most attenuating clutter filter is employed. In this circumstance, large radial velocity estimate biases result as was illustrated in Figure II-5. At short range, roughly 50% of the azimuth sectors at Huntsville would be obscured by ground clutter if microburst reflectivity was 10 dBz. This obscuration is more prevalent towards the northeast and east owing to terrain relief and the presence of man made structures.

As weather reflectivity is increased the area of obscuration decreases rapidly. When the ground clutter residue of the most attenuating clutter filter does not exceed weather power, velocity biases are due to removal of weather echo power by the clutter filters or to clutter breakthrough. As illustrated in Figures II-5 and II-6, velocity biases due to clutter filtering do not typically exceed 2 m/s; in addition, we have set the filter selection decision threshold to a value that makes ground clutter breakthrough infrequent. For a 20 dBz outflow, less than 10% of resolution cells (ensembled over azimuth) are obscured at any range and for a 30 dBz outflow, obscuration is negligible.

Figure IV-5 repeats the obscuration calculations for a microburst signature with only half of the radial velocity shear ($\pm$5 m/s) considered previously. In this situation, more of the resolution cells have near-zero radial velocity. Owing to filter attenuation, this results in increased probability of significant velocity estimate biases or loss of the weather echo signal in noise. For $\pm$5 m/s "microburst" signatures with 20 dBz or 30 dBz reflectivity factors, the probability of obscuration is respectively 25% and 5% at short range. For a 10 dBz event, the obscuration percentage is greater than 50% at all ranges less than 6 km.

As a final example, Figure IV-6 assumes a $\pm$10 m/s shear signature that has larger horizontal dimensions -- 4.8 km or twice that assumed in Figure IV-4. Overall, the fractional obscuration for the larger dimension outflow is similar to that plotted in IV-4. A 10 dBz outflow centered at ranges less than 4 km would be obscured in more than 50% of azimuth sectors. For 20 dBz or greater weather reflectivity factors, this percentage is less than 5% at all ranges.

Overall these calculations with simulated shear signatures indicate that, in the presence of "typical" ASR low-beam ground clutter, operationally significant thunderstorm outflows can be measured at all ranges when the reflectivity factor is approximately 20 dBz or greater. For lower reflectivity wind shear events, the high receiving beam may be required. At very short range -- where ground clutter interference is most severe -- the high beam may still provide accurate low altitude wind measurements [1]. Note however, that receiver sensitivity may prevent high beam measurement of thunderstorm outflow winds when the reflectivity factor is

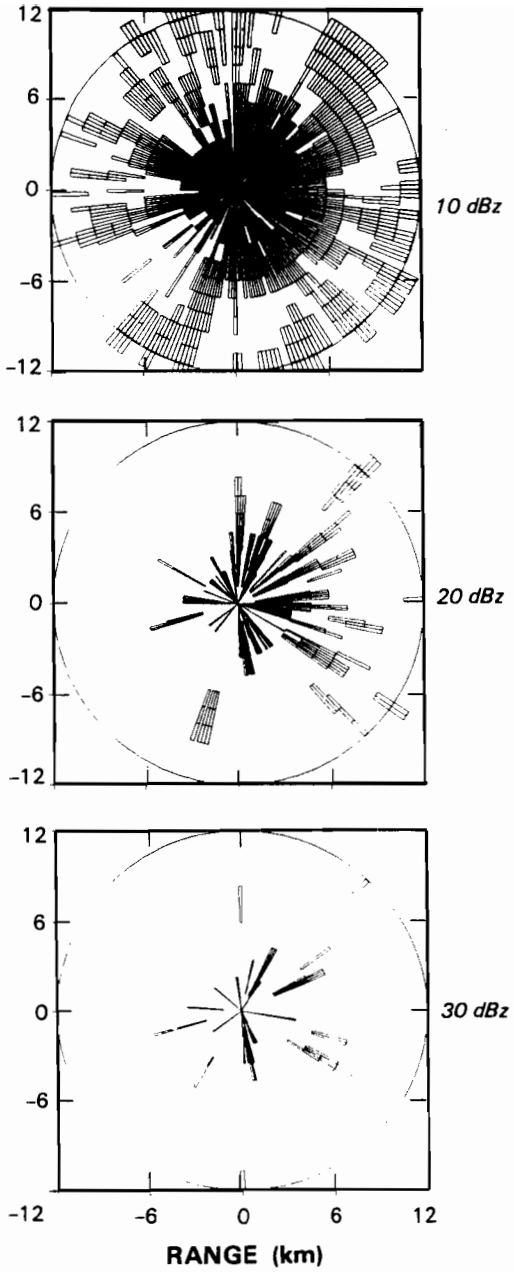

Figure IV-5. Areas of obscuration for a microburst with velocity differential of 10 m/s, no velocity offset and 2.4 km radial extent. Weather reflectivity factors of 10, 20 and 30 dBz are assumed.

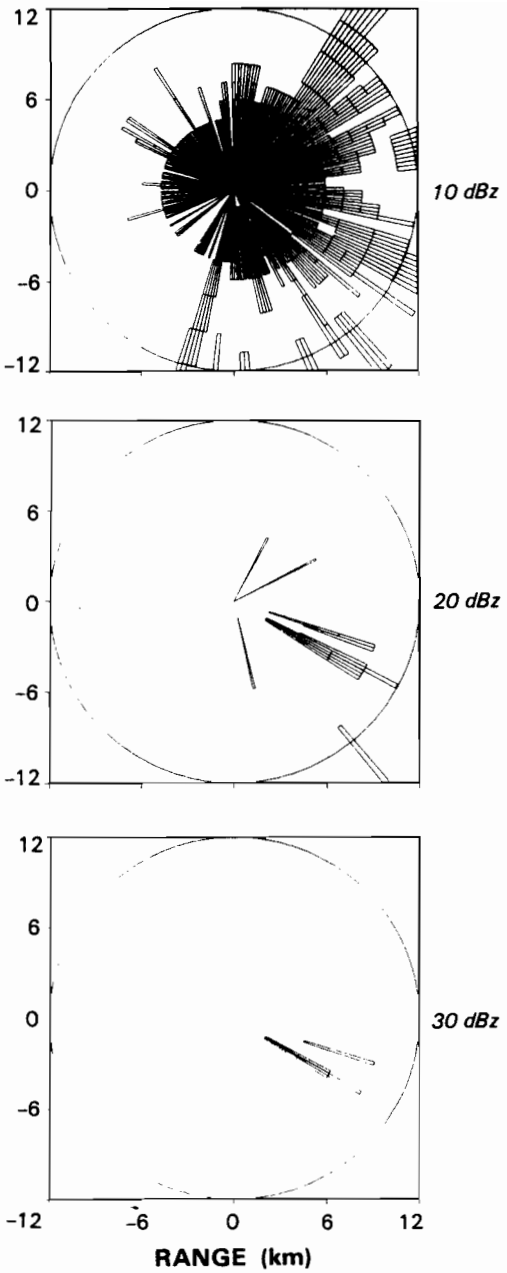

86977-21

Figure IV-6. Areas of obscuration for a microburst with velocity differential of 20 m/s, no velocity offset and 4.8 km radial extent. Weather reflectivity factors of 10, 20 and 30 dBz are assumed.

well below 20 dBz [1].

B. Measurements of Real Weather

We conclude with three examples of reflectivity and wind measurements in rain or thunderstorms at the Huntsville testbed ASR. While it is difficult to quantify the impact of ground clutter when the "true" weather parameters are not known, these case studies provide qualitative support to our conclusion that low beam ground clutter can be adequately suppressed for wind measurements in most storms. We will consider one case involving homogeneous reflectivity and radial velocity and then present examples of linear ("wind-shift line") and radially divergent ("microburst") shear measured with the testbed ASR.

Note that these data were obtained with the radar operating with a constant PRF of 976 s^{-1} rather than the eight/ten pulse block stagger used by the ASR-9. This has been necessary because the testbed radar's transmitter instability residue is only about -33 dB in block stagger mode, providing insufficient ground clutter rejection capability. Modifications to reduce the transmitter instability residue in both constant and staggered PRF mode are in progress. As indicated in Section II, use of the alternating PRF should not affect signal processing performance provided that the clutter filter impulse responses are shift variant.

Figure IV-7 shows radar reflectivity factor and radial velocity estimates from the testbed ASR on 18 January 1987. Light to moderate rain was falling throughout the Huntsville area. Reflectivity factors measured with the testbed ASR at ranges beyond the ground clutter were generally 25 to 40 dBz. Figure IV-7(a) shows pulse-pair reflectivity measurements made without use of ground clutter filtering. The "splashes" of high reflectivity ($>$ 40 dBz) throughout the image represent interference power from ground clutter. Inside 5 km, the weather echo to ground clutter ratio is -20 dB or smaller in many resolution cells.

Figure IV-7(b) displays reflectivity estimates after ground clutter filtering but prior to median filtering. Speckles of high reflectivity throughout the image result from clutter breakthrough caused by temporal changes in clutter intensity as discussed in Section III. We can derive a rough measure of the breakthrough probability by examining the reflectivity and radial velocity fields for simultaneous occurrence of high reflectivity and near-zero radial velocity. For this data set, we declare clutter breakthrough when the reflectivity factor estimate in a resolution cell exceeds 40 dBz *and* the magnitude of the radial velocity estimate is less than 2.0 m/s. In order to make use of this velocity test, the analysis is confined to azimuth sectors where the antenna beam is roughly parallel or antiparallel to the wind vector. Inside 6 km, the resulting measurement of clutter breakthrough probability is 4.4 x 10^{-2}. This is in good agreement with Figure III-6 which shows that clutter breakthrough probability prior to spatial filtering is 3.2 x 10^{-2} for the threshold setting we use (T_2=4.0, see equation 8).

Figure IV-7(c) and (d) display reflectivity and radial velocity estimates formed at the output of the spatial median filter. The images are now largely free of ground clutter breakthrough contamination. The breakthrough probability measured as above is 9.3 x 10^{-3}, again in good agreement with that calculated in Figure III-6. More importantly, the radial velocity field is spatially consistent right up to the radar; the measurements at short range indicate low level flow from the southeast, veering to southwesterly at longer range as the beam accepts power from higher altitudes.

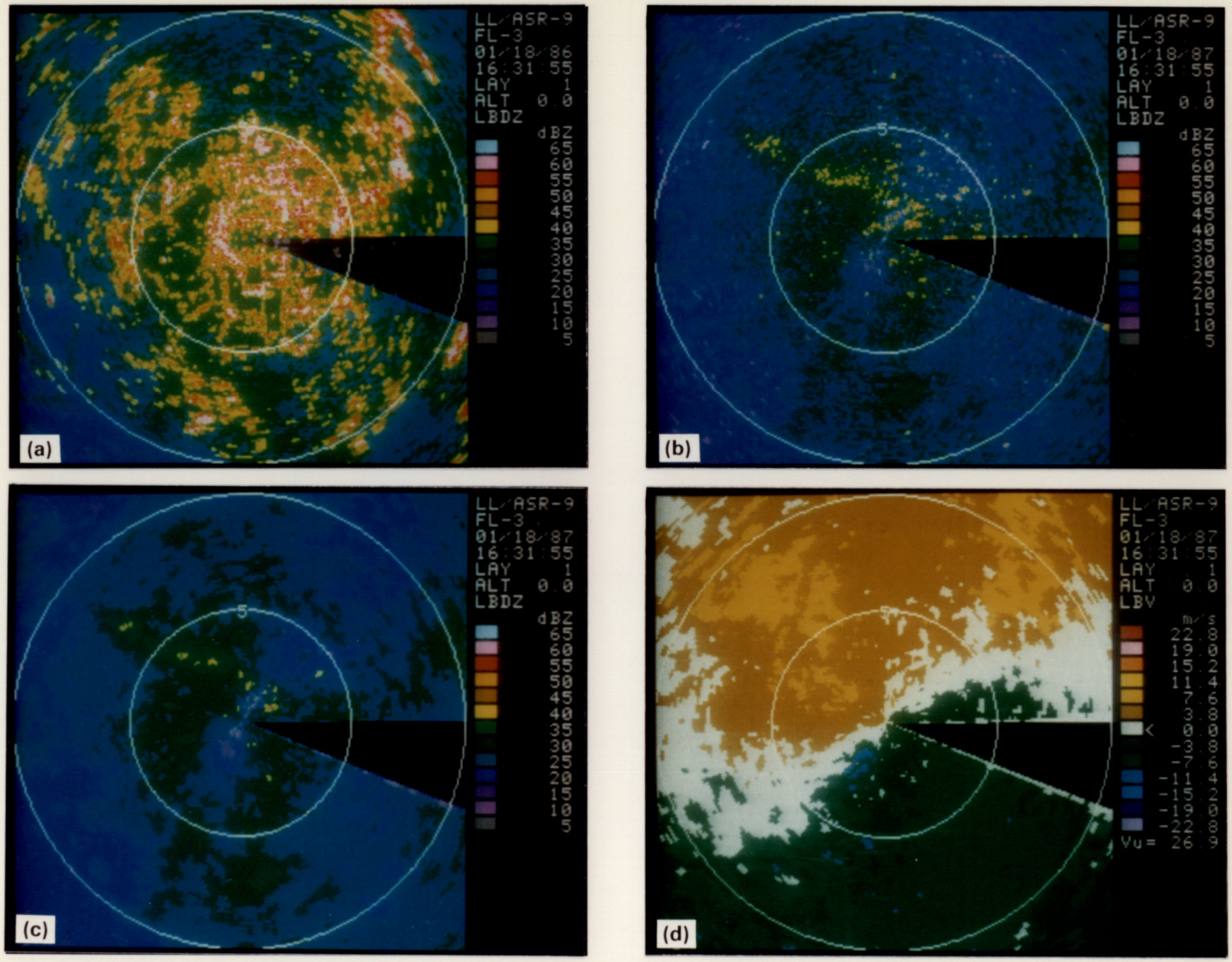

Figure IV-7. (a) Reflectivity field measured with the testbed ASR in a stratiform rain system on 18 January 1987. Clutter filters were turned off for this image. Range rings are at 5 km intervals; (b) reflectivity field after clutter filters but before the spatial median filter; (c) reflectivity field after spatial filtering; (d) radial velocity field after spatial filtering.

Figure IV-8(a) and (b) shows reflectivity factor and radial velocity measurements during a rain storm on 9 December 1986. On this day, lines of heavy precipitation formed within a widespread rain system and propagated at high velocity in a southeasterly direction. The measurements in the figure were made as one of these rain lines passed over the radar. Parts (c) and (d) of the figure are simultaneous measurements from Lincoln Laboratory's S-band TDWR prototype radar (1^o conical beam) scanning at a 3^o elevation angle so as to avoid illumination of ground scatterers. The pencil beam radar was situated within 1 km of the testbed ASR.

Reflectivity factors measured with the ASR are in good agreement with the weather radar measurements at ranges less the 20 km. In particular, there is no visual evidence of ground clutter breakthrough or significant attenuation of the weather echo owing to the clutter filtering process. Reflectivity factors within the line of heavy rain are somewhat underestimated by the ASR at ranges beyond 20 km owing to incomplete filling of the antenna beam.

The velocity fields from both radars show the convergent wind line created by the precipitation. The pencil beam radar measured a velocity difference across this line of 15 m/s at low altitudes (i.e. short range). Comparison of velocity measurements from the two radars shows no evidence of ground clutter contamination in the ASR measurements; the noticeable underestimate of the shear magnitude is a result of the fan-beam's acceptance of power from lower velocity precipitation overhanging the surface boundary layer convergence [1]. In the more vertically uniform wind field ahead of and behind the rain line, radial velocities measured with the two radars are in good agreement. Note that a lower PRF for the pencil-beam radar results in velocity aliasing to the west at ranges greater than 20 km as the beam accepts power from high velocity precipitation aloft.

On 21 May 1987 an intense thunderstorm over the testbed ASR produced two strong divergent outflows (microbursts) during a 15 minute period. Figure IV-9 compares reflectivity and radial velocity measurements from the testbed ASR with measurements from a collocated C-band meteorological Doppler radar (1.4^o beamwidth) provided by the Massachusett Institute of Technology's Weather Radar Laboratory. Parts (a)-(d) show the first outflow (3 km range and 190^o azimuth). Radial shear measured with the pencil beam radar on a 0.7^o PPI scan was 12 m/s over a 1.5 km range extent. The divergent signature is also clearly recognizable in the ASR data which measured an approximately equal velocity differential across the event. The good agreement between the shear measurements with the two radars results because:

(1) the radar reflectivity factor in the microburst was 40-45 dBz so that the impact of ground clutter on the ASR velocity measurements was small (see Figure IV-5);

(2) the microburst outflow winds (as measured by the pencil-beam radar with RHI scans) extend well above the surface (600 m). As shown in reference [1], ASR velocity measurement errors due to weather phenomena above the outflow layer will be minimal when a wind shear event of this height occurs within 5 km of the radar.

Figures IV-9(e)-(h) treat a second outflow centered 8 km east of the radar. The maximum radial velocity differential measured with the ASR was 22 m/s in comparison to a value of 29 m/s measured with the pencil-beam weather radar. RHI scans through this outflow were not performed until about 4 minutes after the time illustrated in the figures. At the later time, these scans showed that the

ASR REFLECTIVITY AND WIND MEASUREMENTS

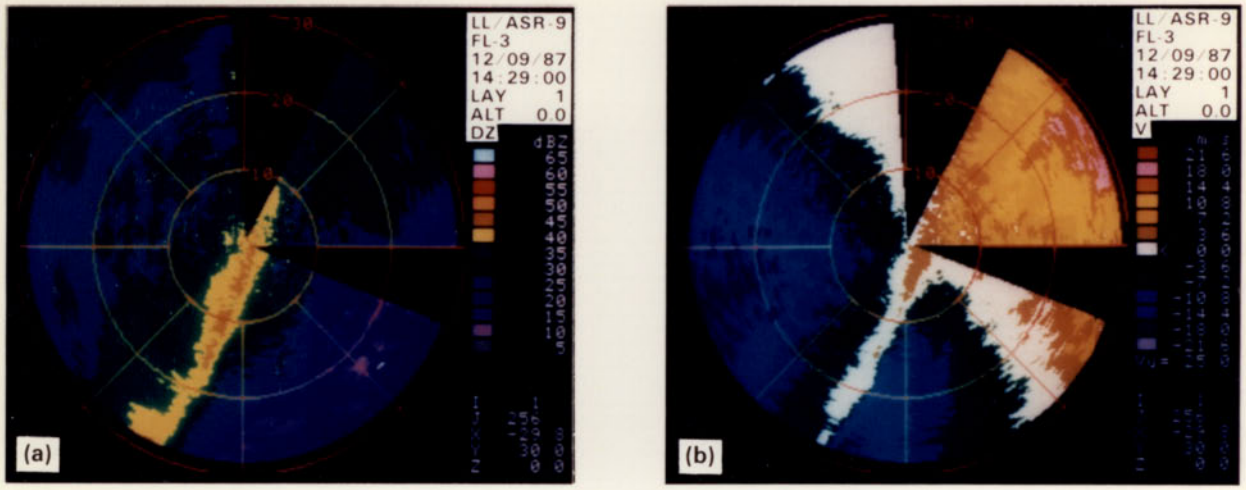

PENCIL BEAM MEASUREMENTS

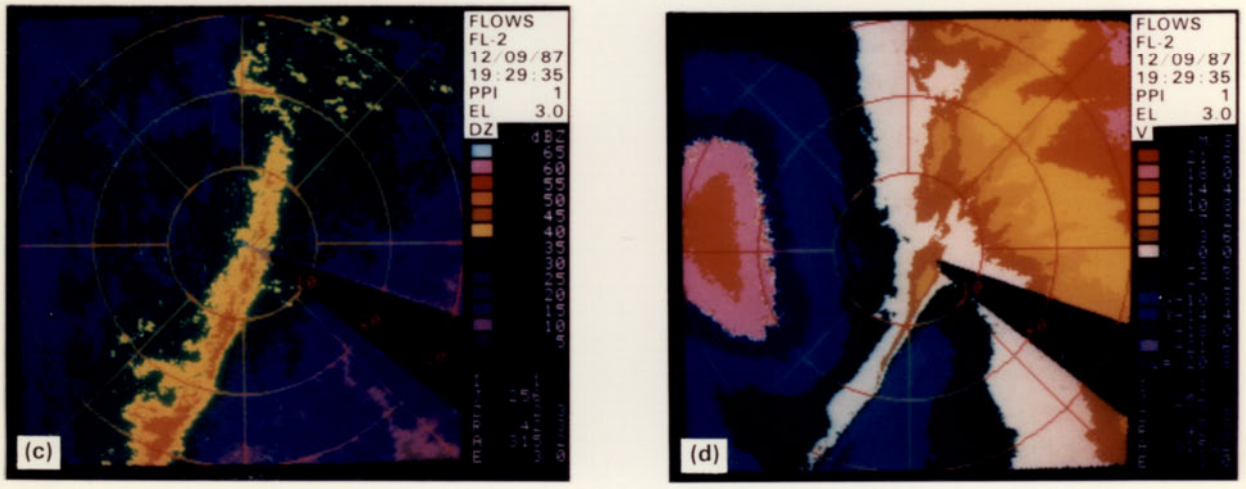

Figure IV-8. Comparison of reflectivity and radial velocity measurements on 9 December 1986 from the ASR testbed and a collocated S-band pencil beam weather radar. Pencil beam radar was scanning at 3.0° elevation angle. Range rings are at 10 km intervals. (a) ASR reflectivity measurements; (b) ASR radial velocity measurements; (c) pencil beam radar reflectivity measurements; (d) pencil beam radar radial velocity measurements.

ASR TESTBED

REFLECTIVITY

RADIAL VELOCITY

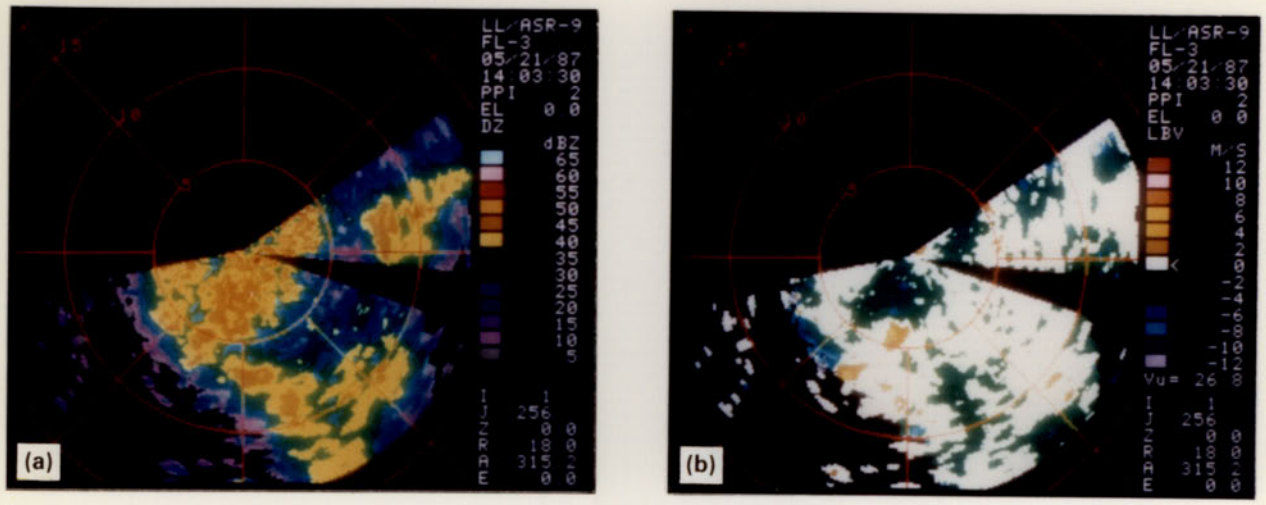

PENCIL BEAM RADAR

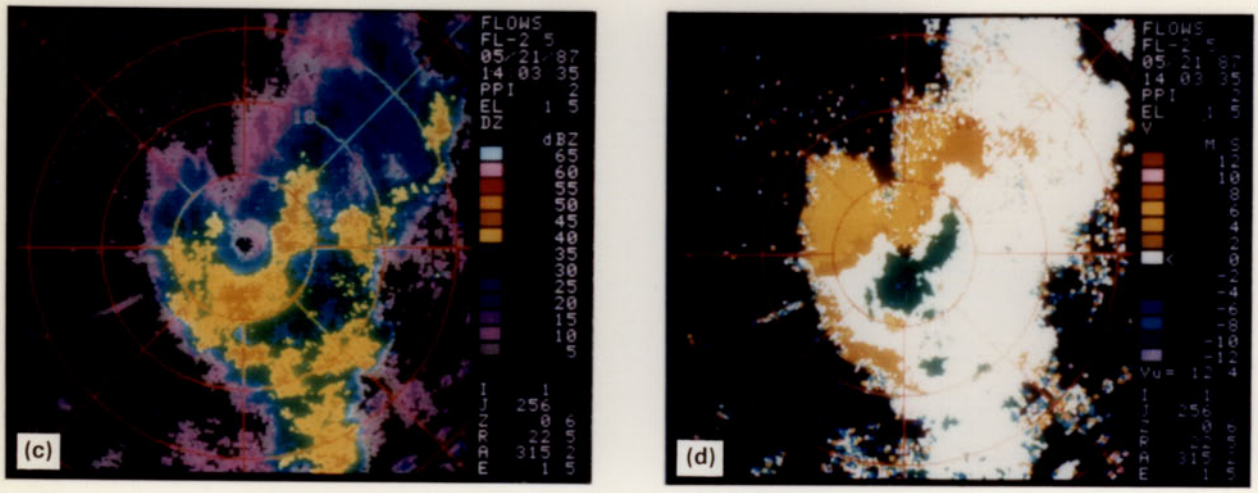

Figure IV-9. Comparison of reflectivity and radial velocity measurements at 14:03 UT on 21 May 1987 from the ASR testbed and a collocated C-band pencil beam weather radar. Pencil beam radar was scanning at 0.7° elevation angle. Range rings are at 10 km intervals. (a) ASR reflectivity measurements; (b) ASR radial velocity measurements; (c) pencil beam radar reflectivity measurements; (d) pencil beam radar radial velocity measurements;

ASR TESTBED

REFLECTIVITY

RADIAL VELOCITY

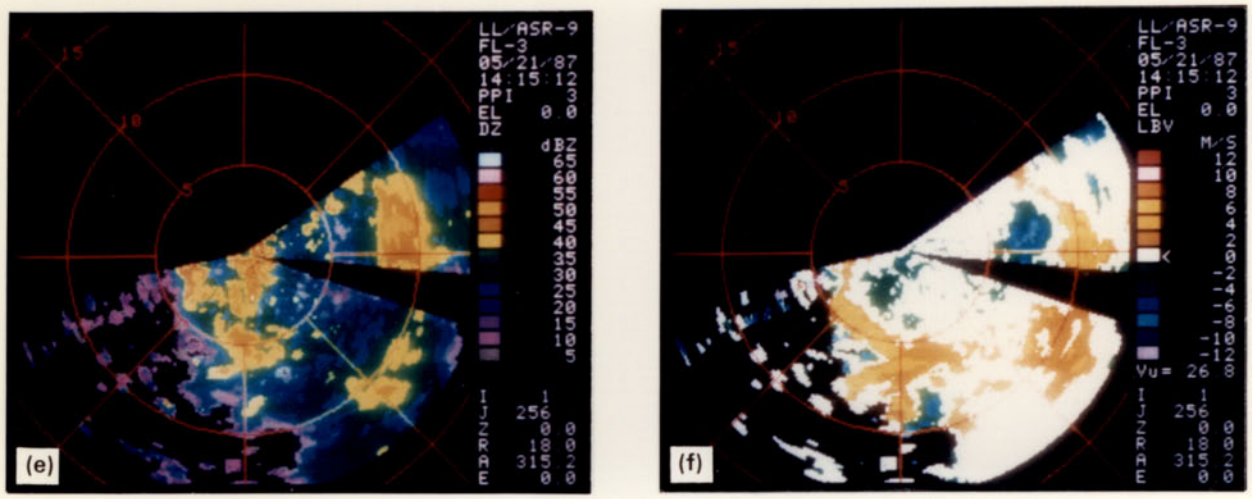

PENCIL BEAM RADAR

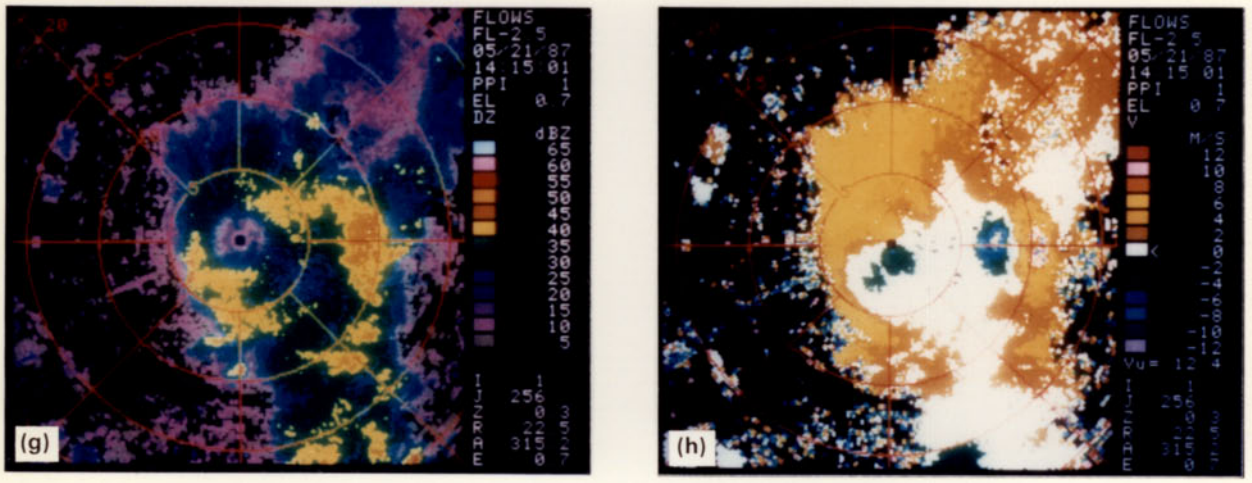

Figure IV-9. Continued. (e) Measurements at 14:15 UT on 21 May 1987. ASR reflectivity measurements; (f) ASR radial velocity measurements; (g) pencil beam radar reflectivity measurements; (h) pencil beam radar radial velocity measurements.

outflow wind pattern extended 600-800 m above the surface. If we accept these measurements as representative of the outflow depth at the illustrated time of peak intensity, calculations of the effect of the ASR's low-beam antenna pattern -- as in reference [1] -- can be performed. These calculations indicate that the lower radial velocity differential measured with the ASR can be attributed to the effect of precipitation scatterers above the microburst outflow layer. The ASR measurements of reflectivity and velocity do not show evidence of ground clutter contamination. This is consistent with the measured reflectivity factors in this microburst and the calculations in Section IV-A.

The above examples illustrate that airport surveillance radars can make useful reflectivity and radial velocity measurements in spite of intense low beam ground clutter at short range. The displayed velocity fields are largely uncorrupted by clutter breakthrough (isolated cells with anomalous reflectivity and zero velocity); in the stratiform rain case where a quantitative measurement of the probability of such breakthrough was feasible, the measured probability showed good agreement with expectations based on the ground clutter analysis described in Section III. Biases in the radial velocity estimates owing to removal of weather echo power by the clutter filters are likewise not in evidence. Such biases would result in velocity field inconsistencies that track areas of heavy ground clutter (i.e. extensive use of the high pass filters). No such anomalies are evident in comparison of the images in this section with the ground clutter display in Figure III-2.

V. SUMMARY AND DISCUSSION

This report supplements previous analysis [1],[4] of the ground clutter rejection requirement for low altitude wind measurements with an airport surveillance radar. We first described a signal processing sequence based on:

(a) a multiple-CPI clutter filtering procedure proposed by Anderson [4];

(b) adaptive selection of the filter transfer function based on the intensity of weather and ground clutter in each resolution cell;

(c) pulse-pair reflectivity and radial velocity estimation;

(d) spatial filtering to reduce the probability of ground clutter breakthrough.

We described a simple filter selection procedure based on a comparison of measured filter output power to a stored value obtained previously under "clutter-only" conditions. An appropriate threshold setting for this comparison was derived.

Clutter measurements from a Lincoln Laboratory testbed ASR were used to evaluate the above processing sequence. We believe that these data are representative (in spatial extent and intensity) of the ground clutter environment expected for operational ASRs. We showed how temporal fluctuations of ground clutter intensity in a resolution cell affect the filter selection procedure, requiring "relaxation" of the filter selection threshold to maintain clutter breakthrough probability at an acceptable level. The data were then used to delineate the conditions (spatial location, weather reflectivity factor, shear magnitude) where ground clutter or the requisite clutter filtering would severely distort measurements of a low altitude velocity shear signature.

We concluded with examples of reflectivity and wind measurements from our testbed ASR, using the processing sequence and parameter settings defined previously. These examples illustrated that the ASR measurements:

(a) are spatially consistent (i.e. there are few "holes" or obvious areas of bias);

(b) are in reasonable agreement with data from collocated pencil-beam radars scanning so as not to illuminate ground clutter;

(c) provide recognizable velocity shear signatures in the operationally significant region within 10 km of an airport.

The conclusions of this report are in agreement with reference [1], indicating that in a representative ASR clutter environment, low-altitude wind shear signatures can be extracted from competing ground clutter when the associated reflectivity factor is approximately 20 dBz or greater. This is normally (but not always) the case for microbursts occurring in moist low altitude air masses such as prevail over the eastern United States during summer. In this environment, errors due to weather phenomena above shallow thunderstorm outflows may often be more significant than ground clutter in limiting the accuracy of wind shear measurements with an ASR [1].

Radar observations of microburst-producing thunderstorms in the western high plains (Denver, CO) indicate that strong surface outflows with reflectivity factors less than 20 dBz occur with some frequency [10]. Ground clutter at such locations may be a significant factor for reliable measurement of wind shear for this class of microbursts. Use of airport surveillance radars to measure winds in very low reflectivity microbursts may require:

(a) careful siting of the radar so as to avoid illumination of clutter sources;

(b) reduction of the radar's transmitter instability residue to allow for greater clutter attenuation than we currently achieve with our testbed ASR.

Gust fronts may also present very low radar cross-sections once they have propagated away from the generating precipitation [11]. Gust fronts are larger scale phenomena, however, and would extend outside the area of intense ground clutter even as they pass over an airport. Thus extrapolation of the wind shift line into the airport area, either temporally or spatially, might be used to estimate a gust front's location even if ground clutter obscured the signature at short range.

The goal of our testbed ASR operations in Huntsville during 1987 is to measure the detection probability and the accuracy of shear magnitude estimates for microbursts and gust fronts in the operationally important region within 15 km of the radar. Our plan is to utilize the signal processing procedures described in this report in combination with a computer algorithm that will automatically identify regions of significant velocity shear. This algorithm is currently under development, starting with the radial shear detection kernels of existing Terminal Doppler Weather Radar (TDWR) algorithms [12],[13].

An understanding of the accuracy of ASR low-altitude velocity shear measurements is important for assessing their use either in a stand-alone mode or in combination with measurements from other sensors (LLWAS, TDWR). RHI scans with the pencil-beam meteorological radar are being performed extensively in order to measure the vertical structure of thunderstorm outflows and the resulting impact on ASR velocity-shear estimates.

As stated above, we do not expect that ground clutter will present a major problem for ASR wind shear detection in Huntsville owing to the generally high reflectivities associated with microbursts in the moist sub-cloud environment. We are currently conducting a simulation-based analysis of the expected performance of an ASR in measuring winds in a dry sub-cloud environment such as Denver, where low reflectivity wind shear events may pose a more difficult problem with respect to ground clutter rejection and system sensitivity. Analysis of wind shear detection algorithm performance in these two environmental regimes should provide the initial data base for a determination of the operational role of ASR wind measurements.

REFERENCES:

1. M.E. Weber and W.R. Moser, *A Preliminary Assessment of Thunderstorm Outflow Wind Measurement with Airport Surveillance Radars,* Project Report ATC-140, Lincoln Laboratory, MIT, FAA-PM-86-38, 1987.
2. T.T. Fujita, *The Downburst,* SMRP Research Paper **210,** University of Chicago, 1985.
3. M.E. Weber, *Assessment of ASR-9 Weather Channel Performance: Analysis and Simulation,* Project Report ATC-138, Lincoln Laboratory, MIT, FAA-PM-86-16, 1986.
4. J.R. Anderson, *The Measurement of Doppler Wind Fields with Fast Scanning Radars,* submitted to J. Appl. Meteorol., 1986.
5. T.R.F. Nonweiler, *Computational Mathematics: An Introduction to Numerical Approximation,* (Ellis Horwood, 1984), 431 pp.
6. J.H. McClellan, T.W. Parks and L.R. Rabiner, *A Computer Program for Designing Optimum FIR Linear Phase Digital Filters,* IEEE Trans. on Audio and Electroacoustics, **AU-21,** 6, pp.506-526, 1973.
7. L. Stevenson, *The Stapleton Microburst Advisory Service Experiment: An Operational Viewpoint,* Final Report DOT-TSC-FAA-85-8, September 1985.
8. J.B. Billingsley and J.F. Larrabee, *Measured Spectral Extent of L- and X-Band Radar Reflections from Wind-Blown Trees,* Project Report CMT-57, Lincoln Laboratory, MIT, ESD-TR-86-153, 1987.
9. H. Urkowitz, *Signal Theory and Random Processes,* (Aptech House, 1983), 715 pp.
10. M.R. Hjelmfelt, *Structure and Life Cycle of Microburst Outflows Observed in Colorado,* submitted to Journal Clim. and Appl. Meteor., 1987.
11. D.L. Klingle, *A Gust Front Case Studies Handbook,* Project Report ATC-129, Lincoln Laboratory, MIT, FAA-PM-84-15, 1985.
12. M.W. Merritt, *Microburst Detection Algorithm,* in NEXRAD Algorithm Report, Joint System Program Office, 1986.
13. H. Uyeda and D.S. Zrnic, *Automatic Detection of Gust Fronts,* Final Report DOT-FAA-PM-85-11, April 1985.